



**University of
Zurich**^{UZH}

**Zurich Open Repository and
Archive**

University of Zurich
Main Library
Strickhofstrasse 39
CH-8057 Zurich
www.zora.uzh.ch

Year: 2013

Silver in geological fluids from in situ X-ray absorption spectroscopy and first-principles molecular dynamics

Pokrovski, Gleb S ; Roux, Jacques ; Ferlat, Guillaume ; Jonchiere, Romain ; Seitsonen, Ari P ;
Vuilleumier, Rodolphe ; Hazemann, Jean-Louis

DOI: <https://doi.org/10.1016/j.gca.2012.12.012>

Posted at the Zurich Open Repository and Archive, University of Zurich

ZORA URL: <https://doi.org/10.5167/uzh-81918>

Journal Article

Accepted Version

Originally published at:

Pokrovski, Gleb S; Roux, Jacques; Ferlat, Guillaume; Jonchiere, Romain; Seitsonen, Ari P; Vuilleumier, Rodolphe; Hazemann, Jean-Louis (2013). Silver in geological fluids from in situ X-ray absorption spectroscopy and first-principles molecular dynamics. *Geochimica et Cosmochimica Acta*, 106:501-523.

DOI: <https://doi.org/10.1016/j.gca.2012.12.012>

1
2 **Silver in geological fluids from in situ X-ray absorption spectroscopy and**
3 **first-principles molecular dynamics**

4
5
6 Gleb S. Pokrovski ^{1*}, Jacques Roux ², Guillaume Ferlat ³, Romain Jonchiere ^{3,5}, Ari P.
7 Seitsonen ⁴, Rodolphe Vuilleumier ⁵, Jean-Louis Hazemann ⁶

8
9
10 1- Géosciences Environnement Toulouse (GET, ex-LMTG), Observatoire Midi-Pyrénées, Université de
11 Toulouse, CNRS, IRD, 14 avenue Edouard Belin, F-31400 Toulouse, France

12 2- Equipe PMM, Institut de Physique du Globe de Paris, 4 Place Jussieu, F-75252 Paris cedex 05, France

13 3- IMPMC, Institut de Minéralogie et de Physique des Milieux Condensés, Université P. & M. Curie
14 (UPMC), UMR CNRS-UPM C-IPGP 7590, 4, Place Jussieu, F-75252 Paris cedex 05, France.

15 4- Physikalisch-Chemisches Institut der Universität Zürich, Winterthurerstrasse 190, CH-8057, Zurich
16 Switzerland.

17 5- Département de Chimie, Ecole Normale Supérieure, UMR CNRS-ENS-UPMC 8640, 24 rue Lhomond,
18 F-75231 Paris, France.

19 6- Institut Néel, CNRS, 25 avenue des Martyrs, F-38042 Grenoble Cedex 9, France

20
21
22 * Corresponding author:

23 phone: (33)-(0)5-61-33-26-18; fax: (33)-(0)5-61-33-25-60;

24 e-mail: gleb.pokrovski@get.obs-mip.fr

25
26
27 **Running title:** Silver in hydrothermal fluids

28
29 **Keywords:** silver; chloride; hydrothermal fluid; X-ray absorption spectroscopy; Ag-Cl complexes;
30 molecular dynamics; XANES; EXAFS; thermodynamic properties; ore deposits

31
32 Revised version # GCA-D-12-00383 for *Geochimica et Cosmochimica Acta*

33 November 2012

ABSTRACT

The molecular structure and stability of species formed by silver in aqueous saline solutions typical of hydrothermal settings were quantified using in situ X-ray absorption spectroscopy (XAS) measurements, quantum-chemical modeling of near-edge absorption spectra (XANES) and extended fine structure spectra (EXAFS), and first-principles molecular dynamics (FPMD). Results show that in nitrate-bearing acidic solutions to at least 200°C, silver speciation is dominated by the hydrated Ag^+ cation surrounded by 4 to 6 water molecules in its nearest coordination shell with mean Ag-O distances of $\sim 2.32 \pm 0.02$ Å. In NaCl-bearing acidic aqueous solutions of total Cl concentration from 0.7 to 5.9 mol/kg H_2O (m) at temperatures from 200 to 450°C and pressures to 750 bar, the dominant species are the dichloride complex AgCl_2^- with Ag-Cl distances of 2.40 ± 0.02 Å and Cl-Ag-Cl angle of $160 \pm 10^\circ$, and the tri-chloride complex AgCl_3^{2-} of a triangular structure and mean Ag-Cl distances of 2.55 ± 0.05 Å. With increasing temperature, the contribution of the tri-chloride species decreases from $\sim 50\%$ of total dissolved Ag in the most concentrated solution (5.9m Cl) at 200°C to less than 10-20% at supercritical temperatures for all investigated solutions, so that AgCl_2^- becomes by far the dominant Ag-bearing species at conditions typical of hydrothermal-magmatic fluids. Both di- and tri-chloride species exhibit outer-sphere interactions with the solvent as shown by the detection, using FPMD modeling, of H_2O , Cl^- , and Na^+ at distances of 3 to 4 Å from the silver atom. The species fractions derived from XAS and FPMD analyses, and total $\text{AgCl}_{(s)}$ solubilities, measured in situ in this work from the absorption edge height of XAS spectra, are in accord with thermodynamic predictions using the stability constants of AgCl_2^- and AgCl_3^{2-} from Akinfiev and Zotov (2001) and Zotov et al. (1995), respectively, which are based on extensive previous $\text{AgCl}_{(s)}$ solubility measurements. These data are thus recommended for chemical equilibrium calculations in mineral-fluid systems above 200°C. In contrast, our data disagree with SUPCRT-based datasets for Ag-Cl species, which predict large fractions of high-order chloride species, AgCl_3^{2-} and AgCl_4^{3-} in high-temperature saline fluids. Comparisons of the structural and stability data of Ag-Cl species derived in this study with those of their Au and Cu analogs suggest that molecular-level differences amongst the chloride complexes such as geometry, dipole moment, distances, and resulting outer-sphere interactions with the solvent may account, at least partly, for the observed partitioning of Au, Ag and Cu in vapor-brine and fluid-melt systems. In hydrothermal environments dominated by fluid-rock interactions, the contrasting affinity of these metals for sulfur ligands and the differences both in chemistry and stability of their main solid phases (Ag sulfides, Cu-Fe sulfides, and native Au) largely control the concentration and distribution of these metals in their economic deposits.

1. INTRODUCTION

There is a growing need for better understanding the silver behavior in hydrothermal systems hosting a major part of Ag resources on Earth. Despite the low abundance of silver in the continental crust (~50 ppb, Rudnick and Gao, 2003), this trace element is enriched in hydrothermal fluids, with concentrations up to ~100 ppm in brines as show fluid-inclusion analyses (e.g., Heinrich et al., 1999; Ulrich et al., 1999; Audétat et al., 2000; Borisova et al., 2012). Although silver usually follows its geochemical analogs, copper and gold, Ag/Cu and Ag/Au ratios in magmatic-hydrothermal deposits vary over 3-4 orders of magnitude. For example, typical Ag/Au mass ratios in porphyry deposits and epithermal adularia-quartz and alunite-quartz deposits, $\sim 1 \div 1000$, are significantly higher than those of Carlin-type, skarn, and orogenic gold deposits, $\sim 0.001 \div 1$ (e.g., Sillitoe and Hedenquist, 2003; Pal'yanova, 2008). Silver also fractionates from gold and copper in vapor-brine systems of magmatic-hydrothermal settings, where Ag partitions preferentially into the saline solution, whereas Au and Cu often enrich the aqueous low-density vapor, as inferred from natural fluid inclusion data and laboratory experiments (Pokrovski et al., 2005a, 2008a; Kouzmanov and Pokrovski, 2012; references therein). Knowledge of the chemical speciation of silver in geological fluids over the range of magmatic-hydrothermal conditions is the primary requisite for modeling Ag transfers in natural vapor-fluid-melt systems, identifying favorable conditions of Ag-bearing minerals formation, and interpreting Ag tenors in different types of deposits. The present contribution is aimed to provide new data on the stoichiometry and structure of aqueous complexes that carry silver in hydrothermal fluids.

Among the three major natural ligands, hydroxide, sulfide, and chloride that transport base and precious metals in saline liquids and vapors, the Cl^- ion is believed to be the principal carrier of Ag, similarly to other base metals (Fe, Zn, Pb), as demonstrated by numerous experimental studies of Ag-bearing mineral solubilities and vapor-liquid and fluid-melt partitioning (e.g., Wood et al., 1987; Zotov et al., 1995; Wood and Samson, 1998; Pokrovski et al., 2005a, 2008a,b; Simon et al., 2008; references therein). The other two ligands, $\text{H}_2\text{S}/\text{HS}^-$ and $\text{H}_2\text{O}/\text{OH}^-$, may contribute to Ag solubility only in fluids

93 characterized by low temperatures and salinities, alkaline pH and/or elevated sulfide contents (e.g.,
94 Webster, 1986; Stefánsson and Seward, 2003; references therein). The effect of less common ligands such
95 as ammonia (e.g., Wood and Samson, 1998), selenide (Akinfiev et al., 2008), bromide and iodide
96 (Gammons and Yu, 1997), which may form strong chemical bonds with the Ag^+ ion, is expected to be
97 weak in typical hydrothermal fluids with low concentrations of these components compared to the far
98 more abundant chloride.

99 There is thus little doubt that chloride complexes play the major role in the hydrothermal and
100 magmatic transport of Ag; however, they have been a subject of rather limited experimental work
101 concerning the exact stoichiometry and thermodynamic stability of these important species. Two major
102 sources of data on Ag-Cl aqueous species are those of Seward (1976) and Zotov et al. (1995, references
103 therein) who carried out systematic measurements of native silver (Ag) and chlorargirite (AgCl) solubility
104 over wide temperature (T), pressure (P) (to 450°C and 1.5 kbar) and Cl concentration (to 7 m NaCl and/or
105 KCl) ranges. Their data indicate that the dichloride AgCl_2^- is likely to be the dominant species to at least
106 2m Cl; the mono-chloride complex AgCl^0 is significant only in dilute solutions (< 0.01m Cl); higher-order
107 chloride complexes (AgCl_3^{2-}) form only in concentrated Cl brines at moderate temperatures. The large
108 stability of AgCl_2^- was confirmed by subsequent solubility work conducted in narrower T-P-composition
109 windows (e.g., Gammons and Williams-Jones, 1995; Akinfiev and Zotov, 1999). Because the
110 thermodynamic properties of the crystalline silver chloride, $\text{AgCl}_{(s)}$, and aqueous AgCl_2^- were believed to
111 be well constrained at $T \leq 300^\circ\text{C}$ from those works, they were used indirectly to derive the formation
112 constants of aqueous HCl^0 and chloride complexes of a number of metals like Zn, Ca, Mn, Pt, Pd, Nd by
113 measuring changes in $\text{AgCl}_{(s)}$ solubility in the presence of the metal cation in moderately-saline solutions
114 (Ruaya and Seward, 1986, 1987; Williams-Jones and Seward, 1989; Gammons, 1995; Gammons and
115 Seward, 1996; Gammons et al., 1996; Tagirov et al., 1997).

116 However, large discrepancies exist on both stability and stoichiometry of Ag-Cl complexes at
117 elevated salt concentrations (> 2m) typical of natural magmatic-hydrothermal fluids. In particular, tri- and

118 tetra-chloride complexes, which are known for silver at ambient temperatures (Martell et al., 2004,) and
119 for many other metals (Fe, Pb, Zn, Cd) both at ambient and hydrothermal conditions (e.g., Wood and
120 Samson, 1998; Martell et al., 2004; Testemale et al., 2009; Bazarkina et al., 2010; references therein),
121 were insufficiently explored for Ag above 100-200°C. Based on the available solubility studies cited
122 above and ambient-temperature data on $[\text{AgCl}_{1-4}]$ complexes from abundant chemical literature (Martell
123 et al., 2004, NIST Critical database 8.0; refs therein), Sverjensky et al. (1997) and Akinfiev and Zotov
124 (2001) have generated two independent datasets of thermodynamic properties of Ag-Cl complexes using
125 the revised Helgeson-Kirkham-Flowers (HKF) model (Tanger and Helgeson, 1988). These datasets are
126 now integrated in computer codes and largely used by geochemists; however, they appear surprisingly
127 inconsistent as shown in Fig. 1. Calculations using these two datasets reveal large differences at $T >$
128 300°C and $m_{\text{Cl}} > 1.5\text{m}$ in the Ag chloride species distribution dominated either by AgCl_2^- (Akinfiev and
129 Zotov, 2001) or AgCl_4^{3-} (Sverjensky et al., 1997). This leads to large discrepancies when predicting Ag-
130 bearing minerals solubility in saline fluids at elevated T, attaining a factor of 10 to 100 in dissolved Ag
131 concentration above 400°C over the acidity and sulfur fugacity ranges typical of natural fluids (Fig. 2).
132 These discrepancies may also affect the thermodynamic data for other metal chloride complexes derived
133 from solubility measurements of AgCl(s) (see above). In addition to the chloride number (also commonly
134 referred to as ligation number), knowledge of species geometry and hydration structure (i.e., presence of
135 water molecules in the Ag coordination shell) is also required to interpret Ag partitioning in brine-vapor
136 systems (Pokrovski et al., 2005a, 2008a). Molecular structures of Ag species are necessary to make sound
137 physical-chemical comparisons with its analogues, Au and Cu, which also form chloride complexes in
138 hydrothermal fluids.

139 In situ X-ray absorption spectroscopy (XAS) provides a direct way to resolve the discrepancies of
140 the Ag-Cl species stoichiometry and to access their structures and hydration numbers. In contrast to its
141 analogs Au and Cu whose major chloride and sulfide complexes in high T-P aqueous solution have
142 recently been investigated using XAS (Fulton et al., 2000; Brugger et al., 2007, Berry et al., 2009;

143 Pokrovski et al., 2009a,b; Etschmann et al., 2010), the only data available for Ag at T above ambient is a
144 XAS study of Ag^+ hydration to 300°C and saturated vapor pressure (P_{sat}) are those of Seward et al.
145 (1996). This cation is however unlikely to play a major role in typical chloride-bearing fluids (see above).
146 Recent improvements in the design of high T-P optical cells for synchrotron (e.g., Testemale et al., 2005)
147 allow now in situ XAS measurements on dissolved metals to supercritical conditions, avoiding the
148 difficulties of classical hydrothermal-reactor techniques related to bulk solubility determination (e.g.,
149 artifacts related to sampling or quenching, Pokrovski et al., 2008b) and its interpretation in terms of
150 dissolved species (e.g., choice of speciation models based on bulk solubility, Pokrovski et al., 2006). In
151 addition, a far more rigorous analysis of XAS data is now possible owing to the progress in quantum-
152 chemistry and molecular dynamics modeling allowing robust constraints on electronic structures, species
153 geometries, hydration shells, and solute-solvent interactions (e.g., Ferlat et al., 2002; Dang et al., 2006;
154 D'Angelo et al., 2008; Sherman, 2010).

155 In this work, we performed in situ XAS measurements (including near-edge structure spectra or
156 XANES, and extended fine structure or EXAFS spectra) on silver chloride aqueous solutions in a wide
157 salinity range (0.7-5.9m Cl) at 200-450°C and 600-800 bar. The data were processed using classical
158 EXAFS analyses, quantum-chemical simulations of XANES, and first-principles molecular dynamics
159 modeling of Ag-Cl-H₂O interactions in aqueous solution. Results provide new speciation and structural
160 data on Ag chloride complexes responsible for the transport of this metal by geological fluids, and allow a
161 better interpretation of the behavior of Ag and associated metals (Au and Cu) in hydrothermal settings.

163 2. MATERIALS AND METHODS

164 2.1. Experimental design and X-ray absorption spectra acquisition

165 XAS measurements were performed on one nitrate $\text{AgNO}_3\text{-HNO}_3$ and three chloride AgCl-NaCl-HCl
166 aqueous solutions, prepared from analytical grade reagents and deionized water. Solution compositions are reported
167 in Table 1 in molality units (m = number of moles of each solute per kg of water). Hydrogen peroxide (0.05-0.10 m
168

169 H₂O₂) was also added in each solution to prevent precipitation of native silver that may happen at elevated
170 temperature (e.g., Seward, 1973). A weighed amount of silver chloride, which is weakly soluble at ambient
171 temperature (< 0.001m), was pressed in pellets and loaded in the experimental cell. Total dissolved silver
172 concentration in solution was measured from the absorption edge height in transmission mode (Pokrovski et al.,
173 2005b, 2009a; Table 1). The solubility of AgCl_(s) increases with temperature (e.g., Seward, 1976), and the
174 acquisition was started $\geq 200^{\circ}\text{C}$ when dissolved Ag concentrations are high enough (≥ 0.01 m) to allow low-noise
175 EXAFS spectra to be obtained in transmission mode (see below). At moderate T (200-300°C), dissolved Ag
176 concentrations attain a steady state value within 10 min. after the temperature reach and remain stable for at least
177 several hours, indicating that equilibrium with AgCl_(s) is likely to be reached. The rapid equilibrium reach is in
178 agreement with previous batch-reactor solubility studies (Seward, 1976; Zotov et al., 1995). However, at T > 300°C
179 and high salinities with large excess of solid phase, Ag dissolved concentrations decreased systematically and
180 AgCl_(s) precipitation occurred on the colder optical windows of the cell at the X-ray beam passage. This was
181 manifested by noisy spectra clearly showing the contribution of the solid whose spectrum is very different from
182 those of solutions. In the experiments reported in this study, this was carefully avoided by using smaller amounts of
183 AgCl_(s), corresponding to under-saturated solutions at T > 300°C. In this case, spectra from solutions show no
184 detectable contribution of AgCl_(s). Thus, AgCl_(s) solubility could only be accurately measured at 200°C for all Cl
185 concentrations and at 300°C for the lowest m_{Cl} concentration (0.7m, Table 1). Although minor losses of Ag from
186 solution owing to AgCl_(s) precipitation in the colder zones of the cell, close to the pistons which are out of the
187 sample space probed by X-rays, were still observed for some experiments above 300°C (Table 1), it did not affect
188 the XAS spectra from solution, demonstrating that no precipitation of AgCl_(s) occurs at the beam passage.

189 XAS spectra from Ag aqueous solutions were collected at the Ag K-edge (~25.5 keV) over the energy
190 range 25.2-26.7 keV on BM29 bending-magnet beamline (Filipponi et al., 2000) at the European Synchrotron
191 Radiation Facility (ESRF, Grenoble, France). The storage ring was operated at 6 GeV with a ~200 mA current. The
192 beam energy was selected using a Si (311) double-crystal monochromator detuned by 30% to eliminate higher-
193 order harmonics. Energy was calibrated using a silver metal foil and setting the maximum of its main-edge
194 spectrum derivative at 25.514 keV. Spectra were recorded in transmission mode using ion chambers filled with Ar
195 gas. Multiple XAS scans were performed on each T-P-composition point, with an acquisition time of ~40 min/scan.
196 Experiments were conducted using a high T-P cell developed at the Institute Néel (Grenoble) and recently

197 described in detail elsewhere (Pokrovski et al., 2005b, 2006, 2009a; Testemale et al., 2005). Both solution and solid
198 were placed in the internal cell that consists of a vertical 1-mm thick glassy-carbon tube and two coaxial sapphire
199 pistons, which delimit the sample space and move in the tube in response to T-P changes. The cell is heated by
200 electrical resistances and placed in a stainless-steel vessel pressurized with helium gas and equipped with beryllium
201 windows for X-ray passage. Temperature in the sample space was controlled within $\pm 5^\circ\text{C}$ by thermocouples
202 attached to the glassy-carbon tube. Pressure was monitored by manometers at the cell exit and the end of pressure
203 line; pressure differences between them do not exceed a few bars.

205 2.2. X-ray absorption spectra analysis

206 EXAFS data analysis was performed with the HORAE and IFEFFIT programs (Ravel and Newville, 2005)
207 and following the recommendations of the International XAFS Society (Sayers, 2000). Details about the reduction
208 procedure can be found elsewhere for similar metals (Pokrovski et al., 2006, 2009a,b). Briefly, energies were
209 recalculated into k-space (\AA^{-1}) with E_0 (i.e., the energy at which k is zero) chosen as the maximum of the first
210 derivative of the main-edge spectrum. Spectra were normalized to the absorption edge height, background removed,
211 weighted by k^n , where $n = 1, 2$ and 3 , and Fourier transformed (FT) over the k range $3.0\text{-}11.6 \text{\AA}^{-1}$ for chloride and
212 $3.0\text{-}10.0 \text{\AA}^{-1}$ for nitrate aqueous samples. The shorter k-range for nitrate solutions is dictated by i) the low amplitude
213 of the Ag-O EXAFS signal at high k-values comparable to the spectral noise, and ii) the presence of multielectron
214 excitations $\text{KM}_{4,5}$ and $\text{KM}_{2,3}$ that appear in the $\chi(k)$ data at 10.3 and 12.7\AA^{-1} (Fulton et al., 2009). In contrast, the
215 EXAFS spectrum of the Ag-Cl contribution dominant in Cl-bearing solutions has a higher signal-to-noise ratio
216 above 10\AA^{-1} and thus is much less affected by the multielectron transitions. This was checked by EXAFS fits of
217 larger k-ranges (up to 13.5\AA^{-1}) for some low-noise spectra; they yielded no changes within errors in the derived
218 structural parameters. Fits were performed in R-space on both real and imaginary parts of the FT contributions to
219 obtain the identity of neighbor atoms, Ag-neighbor distance (R), coordination number (N), and Debye-Waller factor
220 (σ^2) for each scattering path (Table 1). A single nonstructural parameter Δe was varied to account for the difference
221 between the experimental absorption-edge energy and its estimate made by FEFF. To diminish correlations
222 between N and σ^2 , and better account for light (O) versus heavy (Cl) neighbors and multiple scattering paths, fits
223 were performed simultaneously with k-weighting of 1, 2 and 3. The fitted values of structural parameters were
224 identical within errors, with comparable fit qualities at each k-weighting. This is an additional demonstration of

225 both the validity of the chosen structural models and the accuracy of the EXAFS background removal procedure
226 (Ravel and Newville, 2005; Kelly et al., 2008). Theoretical backscattering amplitude and phase-shift functions for
227 Ag-O and Ag-Cl single and multiple scattering paths were computed by the FEFF6 ab-initio code (Zabinsky et al.,
228 1995) using AgNO₃ and AgCl crystal structures (Gibbons and Trotter, 1971; Hull and Keen, 1999). The amplitude
229 reduction factor (S_0^2) was set at 0.75 ± 0.05 as found by fitting the spectra of crystalline Ag₂O, AgNO₃, AgCl, and
230 Ag₂S solids. The effect of inharmonic disorder was accounted using the cumulant expansion method with third- and
231 fourth-order cumulants (c_3 and c_4). Multiple scattering (MS) events within the Ag first coordination shell were
232 tested using the FEFF code, assuming tetrahedral, trigonal pyramidal, and linear geometries around Ag as found in
233 the model compounds.

234 In addition to classical EXAFS analyses, XANES spectra of different Ag-Cl-H₂O molecular clusters were
235 modeled ab-initio based on the experimental EXAFS-derived Ag-Cl and Ag-O distances and geometries found
236 from molecular dynamics (see below) using the FDMNES computer code (Joly, 2001). Details about this approach
237 for aqueous species can be found elsewhere (e.g., Testemale et al., 2004; Pokrovski et al., 2009a, Bazarkina et al.,
238 2010). Very briefly, calculations of theoretical XANES spectra of different cluster's symmetry and geometry were
239 performed using the Finite Difference Method (FDM) with an energy resolution of < 0.1 eV (note that in case of
240 low symmetry, the muffin-tin approximation is not sufficient in the near-edge energy range; Joly, 2001). The
241 obtained spectra, which display almost all possible electronic transitions, are further convoluted with a Lorentzian
242 function with a full width of 6.75 eV (Gamma_hole key in the FDMNES input file) to account for the core-hole
243 lifetime at the Ag K-edge, and a Gaussian function to account for the experimental resolution assumed to be equal
244 to the intrinsic resolution of the (311) monochromator (1.1 eV). The value of energy of the Fermi level (E_{fermi}) was
245 fixed to -3.0 eV based on the examination of the density of states (DOS) of the different electronic levels. Changing
246 the values of E_{fermi} from -6 to 0 eV produces only minor effects on the calculated XANES spectra.

248 **2.3. First-principles molecular dynamics simulations**

249 Three different compositions in the model Ag-NaCl-H₂O system were simulated, each consisting of 128
250 water molecules, 1 Ag⁺, 1 Na⁺, and 2, 3 or 4 Cl⁻ ions. These numbers of Cl⁻ ions correspond to apparent Cl
251 molalities (m_{Cl}) of 0.9, 1.3, and 1.7, respectively, but because of the low Cl/Ag ratios in our systems (from 2 to 4),
252 the concentration of free Cl⁻ not complexed with Ag is much smaller. This should be kept in mind when comparing

253 the FPMD results with XAS data from experimental Ag-Na-Cl solutions, where total Cl/Ag ratios are much higher
254 (from 20 to 100, Table 1). The model with 4 Cl⁻ ions was examined at near-ambient (50°C, 1 bar) and supercritical
255 (380°C, 600 bar) conditions. The models with 2 and 3 Cl⁻ ions were simulated at supercritical conditions only.

256 The stability of Cl⁻-bearing complexes was simulated by inserting pre-formed AgCl_n⁽ⁿ⁻¹⁾⁻ clusters with n = 2
257 to 4. For n = 4, the initial geometric configuration is a tetrahedral complex with Ag-Cl bonds of 2.35 Å and Cl-Ag-
258 Cl angles of 109.5°. For n = 3 and n = 2, the initial configurations were derived from the latter one by removing
259 chlorine atoms. To accelerate the equilibration of the surrounding water molecules, classical molecular dynamics
260 simulations using empirical force-fields were ran for typically 1 ns while keeping fixed the geometry of the AgCl_n⁽ⁿ⁻¹⁾⁻
261 complexes. Cubic periodic boundary conditions were employed. The box sizes were adjusted to reach a pressure
262 value close to the target pressures in the empirical force-field simulations (1 bar at 50°C and 600 bar at 380°C),
263 while being guided by the equation of state of the NaCl-H₂O system (Anderko and Pitzer, 1993; Bakker, 2003). The
264 resulting cubic box sizes are 15.7 Å and 17.8 Å for the system with 4 Cl⁻ at near-ambient and supercritical
265 conditions, respectively, and 18.0 Å and 17.7 Å for the systems with 2 and 3 Cl⁻, respectively. The final
266 configurations obtained at the end of the classical runs were then used as starting configurations for FPMD
267 simulations.

268 The FPMD simulations were carried out within the Density Functional Theory (DFT) framework and
269 the Born-Oppenheimer method using the freely available program package QUICKSTEP/CP2K (VandeVondele et
270 al., 2005a). QUICKSTEP uses a hybrid Gaussian plane-wave (GPW) method (Lippert et al. 1997). A triple-zeta
271 valence doubly polarized (TZV2P) basis set was chosen for oxygen, hydrogen, and chlorine (VandeVondele et al.
272 2005b), whereas the double-zeta valence plus polarization (DZVP) basis set optimized for molecules
273 (VandeVondele et al., 2007) was employed for silver. Core electrons were replaced by the Goedecker-Teter-Hutter
274 (GTH) norm-conserving pseudo-potentials (Goedecker et al., 1996; Hartwigsen et al., 1998; Krack, 2005). A
275 neutralizing background charge was implicitly added for all charged systems. The cutoff for the electronic density
276 was set to a high converged value, 600 Ry, with smoothing for the exchange-correlation contribution
277 (VandeVondele et al., 2005a). The gradient-corrected exchange-correlation functional BLYP (Becke, 1998; Lee et
278 al., 1998) was used in the DFT calculations. This functional is known to provide accurate structural results, e.g.
279 inter-atomic distances are over-estimated by only 1-2% (Sprik et al., 1996). Van der Waals interactions were taken
280 into account using the scheme of Grimme (2006). Constant temperature conditions were imposed by a Nosé-

281 Hoover thermostat chain (Nosé 1984a,b). The time step for the MD simulations was 0.5 fs. The simulations were
282 run for 100 ps at 50°C and for 50 ps at 380°C.

283 MD-EXAFS spectra were calculated from the FPMD trajectories using the FEFF code (Zabinsky et al.,
284 1995) and the methodology detailed in Ferlat et al. (2005). Spherical clusters of a radius of 8 Å centered at the
285 silver atom were extracted every 5 fs, providing a total of 20,000 clusters at 50°C and 10,000 clusters at 380°C. An
286 individual EXAFS signal for each cluster was generated including all the contributions from multiple-scattering
287 paths up to 6 legs. In these calculations, the amplitude reduction factor (S_0^2) was set to 0.75 as obtained
288 experimentally, leaving a single parameter $\Delta\epsilon$ to match the experimental and calculated energy mesh. The
289 scattering potentials were calculated in the muffin-tin approximation, and it has been checked that use of the ab-
290 initio self-consistent field scheme led to almost identical results.

292 3. RESULTS

293 3.1. Analysis of EXAFS spectra

294 3.1.1. Nitrate solutions

295 EXAFS spectra of a Cl-free silver nitrate solution (exp #1, 0.21m AgNO₃-0.10m HNO₃-0.10m
296 H₂O₂), in which the hydrated Ag⁺ cation is dominant, could only be acquired to 200°C, because of the
297 rapid loss of dissolved Ag from solution above that temperature due to the precipitation of native silver,
298 likely caused by the reducing environment of the glassy-carbon cell and/or beam-induced effects common
299 for redox-sensitive metals (e.g., Pokrovski et al., 2009a). The spectra collected at 30, 100, and 200°C (Fig.
300 3), display a single contribution from the first-shell oxygen neighbors without any clearly detectable
301 outer-shell signal or multiple scattering paths. The spectra show both reduction in $\chi(k)$ and FT
302 magnitudes and shift to shorter Ag-O distances with increasing temperature (Fig. 3). This is confirmed by
303 quantitative EXAFS modeling yielding Ag-O average distances from 2.34 to 2.30 Å and number of
304 oxygen neighbors from ~6 to ~4.5 when T increases from 30 to 200°C, whereas DW factors of the Ag-O
305 shell remain constant within errors (Table 1). Neither significant anharmonic effects as approximated by

306 the third- and fourth-order cumulants ($c_3 < 3 \times 10^{-4}$, $c_4 < 5 \times 10^{-5}$), nor presence of two different Ag-O
307 distances were detected within the spectral resolution.

308 The absolute values of R and DW parameters derived in this study are identical within errors to
309 those reported by Seward et al. (1996) using EXAFS spectroscopy for similar nitrate solutions from 20 to
310 300°C at saturated vapor pressure (P_{sat}). Our Ag-O distances at near-ambient temperature, $R_{\text{O}} = 2.34 \pm 0.02$
311 Å, compare favorably with previous ambient-temperature studies of the aqua Ag^+ ion by EXAFS
312 (Yamaguchi et al., 1984a), X-ray and neutron diffraction (Yamagushi et al., 1984b; Sandstrom et al.,
313 1985; Skipper and Neilson, 1989), and large angle X-ray scattering (LAXS, Persson and Nilsson, 2006).
314 Most of these studies report Ag-O coordination numbers around four at ambient conditions, which is
315 consistent with the tetrahedral $\text{Ag}(\text{H}_2\text{O})_4^+$ cation, also suggested from UV spectroscopy (Texter et al.,
316 1983) and theoretical DFT quantum chemistry and molecular dynamics (MD) simulations (e.g., Martinez
317 et al., 1997; Feller et al., 1999; Bernasconi et al., 2004). However, other MD simulations (e.g., Armunanto
318 et al., 2003; Fulton et al., 2009) and recent analyses of Ag L- and K-edge EXAFS spectra of silver
319 perchlorate and nitrate solutions (Fulton et al., 2009) are less categorical about the tetrahedral Ag^+
320 geometry, rather suggesting a five- or six-coordinated Ag^+ in aqueous solution. Although our EXAFS-
321 derived coordination numbers are closer to these values (~5-6 O atoms, Table 1), they exhibit significant
322 errors (± 1.5 atoms at least). We believe that the issue of the Ag^+ - H_2O coordination cannot be resolved on
323 the solely base of EXAFS data, but it will require independent information from XANES spectra, which
324 are more sensitive to the cluster geometry and symmetry, as will be shown in section 3.2. Molecular
325 dynamics simulations of Ag^+ in Cl-free aqueous solution will be presented in a subsequent paper.

327 3.1.2. Chloride solutions

328 EXAFS spectra and their Fourier transform magnitudes of the three studied Ag chloride solutions of
329 0.7, 2.6 and 5.9m total Cl are plotted in Fig. 3a,b. They are different both in phase and amplitude from
330 those of the Ag-O environment in nitrate solution, suggesting the predominance of heavier

331 backscatterers, presumably Cl. Qualitative continuous Cauchy wavelet transforms analyses (CCWT,
332 Munoz et al., 2003) demonstrate that the EXAFS is dominated by the Ag nearest shell composed of Cl
333 atoms without any detectable presence of other types of atoms like O (electronic annex EA-1). No outer-
334 shell neighbors or multiple scattering signals are detectable within the spectral resolution (Fig. 3b, EA1-
335 1). In particular, all analyzed spectra show no detectable contribution from $\text{AgCl}_{(s)}$ that might precipitate
336 at the beam passage (see section 2.1). The spectra from solution are devoid of all features typical of the
337 AgCl solid (strong Ag-Ag contributions in EXAFS, particular shape and magnitude of XANES, and large
338 N and R values, see below). The EXAFS spectra of chloride solutions reveal weak but clearly identifiable
339 variations in both phase and amplitude for the same Cl concentration with T change, and amongst
340 different Cl solutions at a given T, suggesting that the Ag-Cl atomic environment depends on both T and
341 m_{Cl} .

342 This is confirmed by quantitative EXAFS fits (Table 1, electronic annex EA-2), which show that
343 average Ag-Cl distances for concentrated chloride solutions systematically decrease over a range of
344 $\sim 0.05\text{-}0.07$ Å with increasing T (e.g., from 2.49 Å at 200°C to 2.42 Å at 450°C for the 5.9m Cl solution;
345 Fig. 4A). At the same T, the Ag-Cl distance increases slightly with increasing Cl concentration (e.g., from
346 2.38 to 2.44 Å at 400°C/600 bar, when m_{Cl} increases from 0.7 to 5.9m; Fig. 4A). The trend in average
347 number of Cl atoms around Ag (N_{Cl}) is less clear, showing values of 2.0 ± 0.2 atoms at $T \geq 300^\circ\text{C}$ in the
348 whole m_{Cl} range (Fig. 4B). At lower T, N_{Cl} values are somewhat higher, attaining ~ 2.5 for the most
349 concentrated solution (5.9m Cl at 200°C). Note however, that the precise evolution of N_{Cl} with T and
350 salinity may be hidden inside the high intrinsic uncertainties associated with this EXAFS parameter. The
351 DW factors of the Ag-Cl shell (σ^2) do not show significant T trends for any investigated solution, but are
352 systematically higher on average at higher m_{Cl} (e.g., differences attain a factor of 2 between the most
353 dilute and most concentrated solution, despite similar N_{Cl} , see Table 1). In addition to the three major
354 structural parameters above, significant anharmonic disorder in Ag-Cl distances was detected as
355 expressed by the c_3 cumulant (Table 1). Despite large intrinsic uncertainties associated with this

parameter ($\pm 50\%$ of the value itself), its inclusion in the model, particularly for the most concentrated solution, yielded a 2- to 3-fold improvement in fit quality as compared with cumulant-free fits. A rough tendency for the c_3 parameter is a slight decrease with increasing T and decreasing m_{Cl} (with the exception of the 5.9m Cl sample at 200°C, Table 1). The derived EXAFS parameters are distinct from those of the AgCl solid ($R_{\text{Cl}} \sim 2.8 \text{ \AA}$, $N_{\text{Cl}} = 6$; Hull and Keen, 1999) implying a different Ag coordination environment in aqueous chloride solutions.

To the best of our knowledge, this study is the first measurement of the molecular structure of aqueous silver chloride complexes. Our derived Ag-Cl coordination numbers ($N_{\text{Cl}} = 1.8 \div 2.5$) and inter-atomic distances ($R_{\text{Cl}} = 2.37 \div 2.49 \text{ \AA}$) are significantly smaller than those in crystalline ($N_{\text{Cl}} = 6$, $R_{\text{Cl}} \sim 2.8 \text{ \AA}$ at 25°C) and molten ($N_{\text{Cl}} = 3 \div 4$, $R_{\text{Cl}} \sim 2.6 \text{ \AA}$ at 500÷800°C) silver chloride (e.g., Inui et al., 1991; Kawakita et al., 2007). In most inorganic and organic compounds with O/N/Cl/P/S ligands, Ag(I) exhibits a distorted tetrahedral coordination with Ag-Cl distances of 2.5÷2.7 Å (ICSD database, 2010), which are at least 0.1-0.2 Å longer than those of this study. The shorter distances found in solution are in agreement with lower Ag coordination numbers and the absence of first-shell water molecules in aqueous Ag chloride complexes compared to most Ag-bearing solids. Our Ag-Cl distances are in agreement with those predicted by DFT modeling of di- and tri-coordinated Ag-Cl-H₂O clusters (Godinho et al., 2005). The structural parameters derived in our study imply the likely predominance of di-chloride complexes in aqueous solution with some fraction, at low T, of complexes having higher Cl numbers. It is, however, important to note that despite the close Cl coordination numbers found for all solutions at $\geq 300^\circ\text{C}$, Ag-Cl distances and DW factors increase systematically with increasing Cl content. This may suggest the simultaneous presence of different [AgCl₂] geometries and/or the presence, in concentrated saline solutions, of outer Cl⁻ and Na⁺ ions that affect first-shell distances and disorder but are beyond direct detection by EXAFS. Principal component analyses (PCA, Malinowski, 1991); Rossberg et al., 2003) of the investigated EXAFS spectra of Cl solutions indicate two factors necessary to describe the experimental dataset. Although this might further support the presence of two kinds of species in the

381 experimental solutions, PCA on T- and m_{Cl} -series of EXAFS spectra for aqueous complexes may be
382 biased by i) the smoothness of changes in metal-ligand distance and ligation number with Cl content,
383 which leads to the lack of contrast and consequent underestimation of the number of species (e.g.,
384 Bazarkina et al., 2010), and ii) changes in metal-ligand distance and disorder with T for the same species,
385 which may overestimate the number of species. Following these limitations of EXAFS and PCA,
386 independent approaches are necessary to better constrain the species stoichiometry and geometry, as
387 shown in the next sections by analyses of XANES spectra and molecular dynamics modeling.

388 389 **3.2. Quantum-chemical modeling of XANES spectra**

390 Normalized XANES spectra of selected nitrate and chloride solutions are plotted in Fig. 5a. The
391 nitrate samples are characterized by slightly higher absorption edge energies (by ~ 1 eV, defined as the
392 maximum of 1st derivative of the spectrum) and more pronounced white-line amplitudes (feature A in Fig.
393 5a) at $\sim 25,525$ eV ($\sim 1.1 \times$ absorption step) than the chloride samples ($\sim 0.9 \times$ absorption jump). Temperature
394 changes in the nitrate spectra are manifested by a slight decrease of the white-line amplitude, likely
395 reflecting the decrease in the Ag-O coordination number as found from the EXAFS analyses above, and
396 also confirmed by XANES modeling below. XANES spectra of chloride solutions have weakly
397 pronounced white-line amplitudes typical for di-coordinated Cu(I) and Au(I) chloride and sulfide
398 complexes (e.g., Brugger et al., 2007; Pokrovski et al., 2009a,b; Etschmann et al., 2010). The second
399 after-edge resonance at $\sim 25,545 \pm 3$ eV of chloride spectra (feature B in Fig. 5a) is in opposite phase with
400 that of nitrate spectra, in agreement with the change of Ag-O to Ag-Cl environment in saline solutions.
401 Spectra of chloride solutions exhibit small but systematic shifts of the white line low-energy side by 1-2
402 eV towards higher energy with increasing T and decreasing m_{Cl} , which results in narrowing of the white-
403 line width, as exemplified by spectra of 0.7m Cl at 450°C and 5.9m Cl at 200°C in Fig. 5a. All other
404 spectra at intermediate m_{Cl} and T fit in between these two 'end members'. Neither the spectra of nitrate
405 nor chloride samples resemble those of $\text{AgNO}_{3(s)}$ and $\text{AgCl}_{(s)}$ reference compounds having, respectively, a

406 distorted AgO_7 (Gibbons and Trotter, 1971) and a regular octahedral AgCl_6 (Hull and Keen, 1999)
407 geometry. This suggests a different coordination environment of Ag in aqueous solution.

408 In the absence of adequate references for aqueous samples, the interpretation of their XANES
409 spectra is greatly helped by quantum-chemical modeling. Theoretical XANES spectra of $[\text{AgO}_m\text{Cl}_n]$
410 clusters of different geometry (from linear to octahedral, with variable degree of distortion) and
411 stoichiometry ($0 \leq (m, n) \leq 6$) were calculated using the FDMNES program (Joly, 2001) and the
412 experimental Ag-O and Ag-Cl distances from EXAFS and/or FPMD calculations (section 3.3). Variations
413 in these distances within 0.1 \AA as found by EXAFS (section 3.1, Fig. 4) yield only minor changes in the
414 width and amplitude of calculated XANES features, without altering significantly the shapes and energy
415 positions of the main resonances. The effect of H atoms (as water molecules or free protons) and outer-
416 sphere Na/Cl atoms (with Ag-Na and Ag-Cl distances $> 3 \text{ \AA}$) on the calculated spectra was found to be
417 too weak to affect their major features and was thus neglected. Note that the low sensitivity of calculated
418 XANES spectra to all these parameters is due to the poor intrinsic resolution imposed by the large core-
419 hole life time of the electron at Ag K-edge ($\sim 7 \text{ eV}$), so that only major changes of geometry and ligand
420 identity in the Ag nearest shell could be unambiguously identified.

421 Calculated XANES spectra of representative types of Ag-O-Cl clusters are shown in Fig. 5b. Three
422 main features are apparent in this figure. a) The white line (feature A) around $25,525 \text{ eV}$ is higher in
423 energy (by $1\text{-}2 \text{ eV}$) and amplitude ($10\text{-}30\%$) for Ag-O clusters compared with Ag-Cl clusters of same
424 stoichiometries. Its amplitude generally grows from linear or angular AgCl_2 and AgO_2 to tetrahedral-like
425 AgO_4 and AgCl_4 clusters. Octahedral-like AgO_6 and AgCl_6 clusters have spectral shapes different from
426 their tetrahedral counterparts, with white lines of narrower width and smaller amplitude. b) The second
427 resonance (feature B) at $\sim 25540 \text{ eV}$ in $[\text{AgCl}_{2,4}]$ clusters is in opposite phase with that of their $[\text{AgO}_{2,4}]$
428 analogs. Features A and B are very similar to those observed in the experimental spectra of nitrate and
429 chloride solutions (Fig. 5a). c) A shoulder (feature C) appears at $\sim 25533 \text{ eV}$ for mixed AgO/Cl clusters,
430 reflecting the presence of both types of atoms around Ag. This feature is not observed in our experimental

431 Cl solutions; this corroborates the absence of O atoms in the first coordination shell of Ag as deduced
432 from EXAFS analyses (section 3.1) and wavelet transforms (EA-1). The similarity of experimental
433 spectra of Cl solutions with those calculated for low Cl number clusters (Fig. 5a, b) suggests that Ag
434 speciation in our saline solutions is likely to be dominated by di- and tri-chloride species, which is also in
435 line with the EXAFS-derived average Cl numbers (Table 1).

436 Experimental spectra of silver nitrate and chloride solids and silver nitrate solution are compared
437 with FDMNES calculated spectra for selected clusters of different geometries in Fig. EA3. Note a
438 similarity between measured and calculated XANES for $\text{AgCl}_{(s)}$ and $\text{AgNO}_{3(s)}$ compounds (Fig. EA3-1);
439 this further supports the validity of the modeling. Experimental XANES spectra of Ag nitrate solutions
440 are closest to those predicted for tetrahedral-like AgO_4 clusters (Fig. EA3-1), in good agreement with
441 most available literature data (see section 3.1) and our molecular dynamics modeling (which will be
442 reported in a future contribution), suggesting the tetrahedral-like hydrated $\text{Ag}(\text{H}_2\text{O})_4^+$. Moderate
443 distortions in Ag-O distances ($\sim 0.1 \text{ \AA}$) and symmetry of $\text{Ag}(\text{H}_2\text{O})_4^+$ from a regular tetrahedron as
444 identified by this and some previous studies could not however be confirmed unambiguously by XANES
445 modeling owing to the insufficient spectral resolution at the Ag K-edge.

446 Experimental spectra of the two most contrasting chloride solutions (0.7m Cl at 450°C and 5.9m Cl
447 at 200°C) are compared with those of representative Ag-Cl clusters in Fig. 6. XANES spectra from the
448 low-concentrated chloride solution (0.7m Cl) at 400 and 450°C resemble most closely those of the
449 $[\text{AgCl}_2]$ cluster with ClAgCl angles around 150-160° (Fig. 6a). A linear AgCl_2 geometry ($\angle \text{ClAgCl} =$
450 180°) yields white-line shapes somewhat steeper and sharper than the experimental spectrum.
451 Furthermore, a linear geometry of the Cl-Ag-Cl bonds would produce significant multiple scattering (MS)
452 contributions in EXAFS spectra, as indicated by FEFF calculations of this study and observed for the
453 quasi-linear di-chloride complexes $\text{Cu}(\text{I})\text{Cl}_2^-$ ($\angle \text{ClCuCl} \geq 160^\circ$, Brugger et al., 2007) and linear
454 $\text{Au}(\text{I})\text{Cl}_2^-$ (Pokrovski et al., 2009b). Our EXAFS spectra do not show such MS features (Fig. 3b),
455 implying a bend geometry, in better agreement with the XANES results. Angles $\text{ClAgCl} \leq 120^\circ$ of the

456 [AgCl₂] cluster yield too flat white-line resonances to be compatible with experimental spectra (Fig. 6a).
457 The experimental spectrum of the most concentrated Cl solution at the lowest T (5.9m Cl, 200°C) has a
458 shape between those predicted for a [AgCl₂] cluster with a ClAgCl angle of 150° and a trigonal pyramidal
459 or plane [AgCl₃] cluster with ∠ClAgCl between 120 and 100° (Fig. 6b). A better geometry resolution
460 within a given Ag:Cl stoichiometry is not achievable from our XANES spectra at the Ag K-edge. In
461 contrast, tetra-coordinated [AgCl₄] clusters yield spectra with narrower and more intense white lines,
462 yielding less satisfactory match of the experimental spectra.

463 This analysis indicates that moderately concentrated solutions are likely to be dominated by the di-
464 chloride complex, AgCl₂⁻, in agreement with the EXAFS-derived Cl numbers of 2, whereas the most
465 concentrated solutions at low-T contain a mixture of di and tri-coordinated Ag-Cl complexes, which is
466 also consistent with the EXAFS-derived Cl numbers of ~2.5 for experiment #5 of 5.9m Cl at 200°C
467 (Table 1). All other solutions at intermediate T and/or m_{Cl} fall in between these XANES shapes. A deeper
468 insight into the species geometry and solvation environment is provided by molecular dynamics as
469 discussed below.

471 3.3. First-principles molecular dynamics simulations

472 The FPMD simulations starting from initial cluster geometries (see section 2.3) were ran for times
473 long enough to visualize the cluster reorganization, i.e. exchange of H₂O molecules and Cl atoms in the
474 nearest Ag environment. Analyses of MD trajectories (e.g., Fig. EA4-1) allow different silver-chlorine
475 complexes to be identified, depending on T and m_{Cl}. The stable complexes found are shown in Fig. 7.
476 Radial and angular distribution functions for these complexes were extracted from subsets of the FPMD
477 trajectories (e.g., Fig. 8 for AgCl₂⁻).

478 At the near-ambient temperature (50°C), several different species persist along our 100 ps
479 trajectory: AgCl₄³⁻, AgCl₃(H₂O)²⁻, AgCl₃²⁻, and AgCl₂⁻ (see Fig. EA4-3). In all these complexes, the
480 chlorine atoms form a well-defined first coordination shell around Ag, well separated from the subsequent

481 water hydration shells (e.g., Fig. 8a). The closest shell of water molecules is found at ~ 3.5 Å from the
482 silver atom at all temperatures; more distant hydration shells cannot be clearly distinguished (Fig. 8a),
483 reflecting the looseness of such long Ag-H₂O bonds and dynamic nature of solute-solvent interactions.
484 Outer shell water molecules at distances above 3 Å from the metal atom were also reported using MD
485 simulations for Cu di-chloride (Sherman, 2007) and Au hydrogensulfide (Liu et al., 2011) complexes. All
486 along the simulation, the Na⁺ ion is found far away, i.e. at least 6 Å, from the silver atom (Fig. EA4-3).
487 The AgCl₄³⁻ complex is a highly distorted tetrahedron with two Cl atoms at an average Ag-Cl distance of
488 2.44 Å, and the two other Cl atoms being at a much larger distance from Ag (3.48 Å). The species
489 AgCl₃(H₂O)²⁻ (resembling AgCl₄³⁻ in which one of the remote Cl is replaced by a water molecule) appears
490 to be an intermediate complex between the “anhydrous” AgCl₄³⁻ and AgCl₂. Anhydrous AgCl₃²⁻ is a
491 trigonal planar complex with a Ag-Cl average distance of 2.60 Å and Cl-Ag-Cl angles of 118°. Finally,
492 AgCl₂⁻ is a slightly bend complex with an average R_{Ag-Cl} of 2.43 Å and a Cl-Ag-Cl angle of 168°. Note,
493 however, the significant scatter in the Cl-Ag-Cl angular distribution, attaining $\pm 10^\circ$ at 1 σ confidence level
494 (Fig. 8b). The slightly different from linear Cl-Ag-Cl angles in the di-chloride complex revealed by MD
495 are in better agreement with the EXAFS and XANES modeling above. Similar angles ($\sim 160^\circ$) were found
496 for AgCl₂⁻ by Liu et al. (2012) in their MD study. Deviations by 10-20° from a linear geometry were
497 detected by XANES spectra modeling of the Cu(I)Cl₂⁻ species in saline solutions similar to those of the
498 study (Brugger et al., 2007).

499 Note that our optimizations of the AgCl₂⁻ cluster in vacuum (i.e., without water molecules) revealed
500 a linear Cl-Ag-Cl angle ($179 \pm 1^\circ$) both at 0 and 300 K. This finding is also in line with static DFT
501 quantum-chemistry calculations both in vacuum or using polarized continuum models for AuCl₂⁻
502 (Pokrovski et al., 2009b) and CuCl₂⁻ (Zajacz et al., 2011) that predict linear geometries ($180 \pm 2^\circ$) for these
503 species. However, optimizations of the full system (AgCl₂⁻ with water molecules) systematically show a
504 non-linear (168°) geometry of AgCl₂⁻, even at 0 K, clearly demonstrating that this is a result of
505 interactions of the AgCl₂⁻ cluster with surrounding water molecules.

506 The angular structure of AgCl_2^- revealed by MD simulations yields a non-zero dipole moment
507 (~ 1.87 debye) for this species, as calculated from maximally localized Wannier orbitals (Marzari et al.,
508 2012) for 30 snapshots extracted from the trajectory. This dipole value, comparable to that of an isolated
509 water molecule (Silvestrelli and Parrinello, 1999) may be responsible for the stronger interactions of
510 AgCl_2^- than its Cu and Au analogs with surrounding water molecules. However, quantitative assessment
511 of the strength of solute-water interactions for Cu, Ag, and Au would require more systematic
512 comparative studies of these metals using similar modeling approaches.

513 As the temperature increases from 50 to 380°C, the average $R_{\text{Ag-Cl}}$ in AgCl_2^- increases from 2.43 to
514 2.45 Å, while the Cl-Ag-Cl average angle decreases from 168 to 159°. For all the trajectories obtained at
515 380°C, AgCl_2^- is found to be the most stable species. Simulations using either AgCl_3^{2-} or AgCl_4^{3-} as
516 starting clusters showed their rapid (in less than 1 ps) dissociation to AgCl_2^- plus one or two hydrated
517 chlorine atoms. For the least concentrated Cl solution, the neutral $\text{AgCl}(\text{H}_2\text{O})$ complex was also found as
518 an intermediate species with a typical life-time of 15 ps for a total simulation time of 50 ps (Fig. EA4-2).
519 In contrast with the absence of Na^+ ions at distances shorter than 6 Å at 50°C (see above), Na^+ was
520 detected in the vicinity of $\text{AgCl}(\text{H}_2\text{O})^0$, at distances between 3 and 4 Å from Ag (Fig. EA4-3).

521 In summary, the AgCl_2^- complex is found at all conditions explored here, confirming the large
522 stability of this species. This conclusion is in agreement with the recent theoretical MD study of Liu et al.
523 (2012). However, in contrast to their study, we found persistence of the AgCl_3^{2-} or AgCl_4^{3-} complexes at
524 moderate chlorine concentrations and low temperatures, in agreement with the present experimental XAS
525 results. The stability of the AgCl_4^{3-} complex is likely to have been overlooked by Liu et al. (2012)
526 probably because of the smaller system size (48 water molecules) used in their study. It should be kept in
527 mind that because of the finite duration of any FPMD simulation, an exhaustive determination of all
528 possible species cannot be guaranteed. Quantifying the relative fractions of each species directly from the
529 trajectories is beyond the reach of modern ab-initio MD simulations. Nonetheless, our simulations help to

530 test independently the stability of some selected species and to calculate their MD-EXAFS spectra, which
531 may directly be compared with experimental data.

532 Typical MD-EXAFS spectra were generated for the complexes identified above using their
533 corresponding subsets of trajectories. Fig. 9 compares the calculated MD-EXAFS spectrum of AgCl_2^- at
534 380°C with the experimental spectrum at close conditions (exp#6, $400^\circ\text{C}/750$ bar, $m_{\text{Cl}^-} = 0.70$). The slight
535 frequency shift between the two spectra visible in this figure is due to the known overestimation of the
536 Ag-Cl nearest distances by typically 0.03 \AA by FPMD calculations using the BLYP functional, as
537 mentioned above (section 2.3). Except for this small difference, the very good agreement in shape, phase,
538 and amplitude of the EXAFS signals between theory and experiment is both a robust validation of the
539 numerical FPMD model and a confirmation of the predominance of AgCl_2^- at these temperature and
540 chlorine concentration.

541 The MD-EXAFS spectra shown in Fig. 10a illustrate the effect of temperature for AgCl_2^- . It can be
542 seen that changes in the signal frequency between 50 and 380°C are very small, implying a weak effect of
543 temperature on EXAFS spectra, which is mainly a result of slight variations in the Ag-Cl coordination
544 shell (Fig. 8a). By contrast, more marked phase shifts are visible at a given temperature between the
545 spectra of AgCl_2^- and AgCl_4^{3-} on one hand, and AgCl_3^{2-} on the other (Fig. 10b). The phase shift of the
546 AgCl_3^{2-} spectrum to lower frequencies is due to longer Ag-Cl average distances in this complex (2.60 \AA)
547 compared to those in AgCl_2^- (2.43 \AA) and the two shortest distances in AgCl_4^{3-} (2.47 \AA). Note that the two
548 longest Ag-Cl distances in the latter species (3.48 \AA) have negligible contribution to EXAFS. The MD
549 calculated phase shifts are in excellent agreement with experimental EXAFS spectra (Fig. 3) suggesting a
550 growing contribution of AgCl_3^{2-} with decreasing T and increasing m_{Cl^-} . In addition, the MD calculated Ag-
551 Cl distances for the dichloride AgCl_2^- (2.38 \AA , when corrected to the typical shift of 2% of the R value,
552 see section 2.3) are identical to those derived from EXAFS fits of the 0.7m Cl solution, confirming again
553 the predominance of this species at elevated temperatures and moderate salt contents.

4. DISCUSSION

4.1. Structure and stability of Ag-Cl complexes in saline solutions

The complementary EXAFS, XANES, and FPMD analyses reported in this study put new important constraints on the stoichiometry and stability of silver chloride complexes at elevated temperatures. The number of Cl atoms derived from EXAFS, the shape of XANES spectra, and molecular dynamics simulations, all converge to the predominance of dichloride complexes with minor contributions of tri-chloride and/or tetra-chloride, at least between 300 and 450°C and chloride concentrations below 3m. The fractions of these higher-order chloride species in the total dissolved amount of Ag for each T-P-m_{Cl} point of our study may be independently estimated either from the experimental mean Ag-Cl coordination numbers or from Ag-Cl distances derived from EXAFS fits and coupled with the data on each individual species coordination number and distance from FPMD modeling (Table 2). In these calculations, we adopted Ag-Cl distances of 2.38 ± 0.01 and 2.60 ± 0.05 Å for AgCl_2^- and AgCl_3^{2-} , respectively. Note that the percentage of the AgCl_4^{3-} species cannot be evaluated using this approach because only the two nearest Cl atoms at ~ 2.4 Å in this species are unambiguously detected by EXAFS, whereas the two other Cl atoms at longer distances (~ 3.4 Å, Fig. 7) give negligible EXAFS signal. Consequently, the tetra-chloride species is almost identical in its EXAFS pattern to the di-chloride complex (e.g., Fig. 10). It can be seen in Table 2 that the fractions of AgCl_3^{2-} in the total dissolved Ag derived from the N and R values are in agreement with one another within errors and do not exceed 20-30% in all experiments at $T > 300^\circ\text{C}$. At 200 and 300°C, these fractions are somewhat higher for most concentrated salt solutions, up to $\sim 50\%$, but the associated uncertainties do not allow more precise estimations.

These EXAFS-derived fractions of AgCl_3^{2-} may also be compared with those calculated using thermodynamic properties of silver cation and its four chloride complexes reported in the literature. Note that according to all data sources, Ag^+ , AgCl^0 , and AgOH^0 fractions are less than 0.1% under our

580 experimental conditions, and thus dissolved silver is shared between AgCl_2^- and $\text{AgCl}_3^{2-} \pm \text{AgCl}_4^{3-}$ (e.g.,
581 Fig. 1). Our tri-chloride species fractions are in marked disagreement with the speciation scheme of
582 Sverjensky et al. (1997) that yields too large percentages of higher-order chloride species, AgCl_3^{2-} and
583 AgCl_4^{3-} , which are inconsistent with the EXAFS and FPMD results (Table 2). Similarly, the fractions of
584 AgCl_3^{2-} derived from the EXAFS parameters are systematically smaller at 200°C and 300°C in 2.6 and
585 5.9m Cl than those calculated using Seward's (1976) stability constants (40-70% AgCl_3^{2-} , Table 2). In
586 contrast, the EXAFS-derived fractions are similar within errors in the whole temperature range to those
587 calculated using the data for AgCl_2^- from Akinfiev and Zotov (2001) and for AgCl_3^- from Zotov et al.
588 (1995). The above comparison thus suggests that AgCl_2^- is likely to be the dominant species in the
589 investigated T and m_{Cl} range, together with some contribution of AgCl_3^{2-} whose fraction diminishes
590 rapidly with increasing temperature and decreasing salinity.

591 Solubilities of $\text{AgCl}_{(s)}$ measured in situ from the absorption edge height of spectra at 200 and 300°C
592 in this study (Table 1) provide an independent confirmation of these conclusions. It can be seen in Fig. 11
593 that the XAS-measured solubilities (Table 1) at 0.7 and 2.6m Cl are close to those predicted using the
594 thermodynamic properties of AgCl_2^- from Akinfiev and Zotov (2001) or Zotov et al. (1995) and assuming
595 that it is the major species formed. Other data for AgCl_2^- (not shown, Seward et al., 1976; Sverjensky et
596 al., 1997) yield comparable (within errors) solubility values at such low-to-moderate Cl concentrations.
597 At higher Cl (5.9m), the XAS solubilities are 2-3 times higher than those predictions, implying a
598 contribution from higher-order Cl species. However, inclusion of AgCl_3^{2-} from Seward (1976) or AgCl_3^{2-}
599 plus AgCl_4^{3-} from Sverjensky et al. (1997) yields $\text{AgCl}_{(s)}$ solubilities at least 2 times higher than the XAS-
600 measured values in the whole m_{Cl} range (Fig. 11). Thus, the stability of tri- and tetra-chloride complexes
601 is likely to be overestimated at $T \leq 300^\circ\text{C}$ in those studies. At $T \geq 300^\circ\text{C}$, the large stability of AgCl_3^{2-} and
602 AgCl_4^{3-} predicted using Sverjensky et al.'s (1997) data is also incompatible with i) the EXAFS-derived Cl
603 numbers of $\sim 2.0 \pm 0.2$ (Table 1), ii) the instability of $[\text{AgCl}_3]$ and $[\text{AgCl}_4]$ clusters revealed by molecular
604 dynamics at 380°C (section 3.3), and iii) $\text{AgCl}_{(s)}$ solubility measured in situ in the 0.7m Cl solution at

300°C (0.049m, Table 1, versus 0.11-0.15m according to Sverjensky's or Seward's data). In contrast, our solubilities in the whole range of m_{Cl} at 200°C (Fig. 7) and in 0.7m Cl solutions at 300°C (Table 1) are in agreement, within better than 30% of the value, with thermodynamic predictions using AgCl_2^- and AgCl_3^{2-} properties from Akinfiev and Zotov (2001) and Zotov et al. (1995), respectively.

The fraction of the tetra-chloride species, detected by FPMD simulations at 50°C and 1.7m Cl, can be estimated neither from XAS data because of its spectral pattern very similar to that of AgCl_2^- (see above), nor from published AgCl(s) solubility measurements because of the absence of reported stability constants for AgCl_4^{3-} above 100°C in solutions of $< 3\text{m Cl}$ (e.g., Seward et al., 1973). Nonetheless, two general criteria may be used to reject AgCl_4^{3-} from the Ag speciation scheme at elevated temperatures and concentrated Cl solutions: a) the long Ag-Cl distances, 3.5 Å, for two of the four Cl atoms as found by FPMD at 50°C, are unlikely to persist at higher temperatures even in highly concentrated salt solutions because of the growing thermal disorder; b) the large negative charge of -3 of this complex will not be favored by the decreasing dielectric constant of the solution when T rises. Thus, AgCl_4^{3-} is not stable and structurally defined enough to be considered as an individual silver complex at temperatures above 50-100°C. It may rather be regarded as AgCl_2^- exhibiting outer-sphere interactions with free Cl^- and/or Na^+ ions in saline solutions. Note that the presence of Na^+ in the outer coordination sphere of Ag ($R_{\text{Ag-Na}} > \sim 3$ Å) is unlikely to be seen by XAS because of high thermal/structural disorder and loose Ag-Na bonds in such outer-sphere complexes, but it is detected by the MD-XAS calculations at $m_{\text{Cl}} < 2\text{m}$ (see above). Thus, despite their relatively simple nearest-shell stoichiometry and geometry, the major silver complexes, AgCl_2^- and AgCl_3^{2-} , are expected to exhibit significant interactions with the solvent and electrolyte in aqueous solution. This may account, at least partly, for the differences in the behavior of silver versus accompanying metals in hydrothermal fluids (section 4.3).

The discussion above allows for the following conclusions: 1) The majority of thermodynamic datasets for the dichloride species, AgCl_2^- (Seward, 1973; Zotov et al., 1995; Sverjensky et al., 1997; Tagirov et al., 1997; Akinfiev and Zotov, 2001) are in fair agreement with one another as well as with the

630 dominant stoichiometry [Ag:Cl₂] inferred in this study at elevated T and low-to-moderate Cl contents. 2)
631 The fraction of the tri-chloride species is likely to decrease fast with increasing T and decreasing salinity,
632 in agreement with previous solubility data (Seward, 1976; Zotov et al., 1995). 3) The stability constants of
633 AgCl₃²⁻ and AgCl₄³⁻ reported in the SUPCRT (Sverjensky et al., 1997) and other related databases (e.g.,
634 LLNL, Parkhurst and Appelo, 1999), which are all based on extrapolations from limited low-T data, are
635 likely to be overestimated and should not be used above 100-200°C. 4) Based on the results of our study,
636 we recommend the use of the stability constants of AgCl₃⁻ from Zotov et al. (1995), to at least 300°C, and
637 AgCl₂⁻ from Akinfiev and Zotov (2001), at least in the T range 200-450°C. This dataset shows the best
638 agreement with the XANES and EXAFS spectra and FPMD simulations of this work and AgCl(s)
639 solubility of this and previous studies.

641 **4.2. Comparison with other metals**

642 The first experimental data for silver chloride complexes at hydrothermal conditions obtained in this
643 study allow comparisons with Ag analogs, Cu and Au, and other metals common in geological fluids. The
644 three metals, Cu, Ag, and Au, are monovalent in hydrothermal fluids and form predominantly single-
645 charged di-chloride complexes at T above 250-300°C (e.g., Akinfiev and Zotov, 2001; Brugger et al.,
646 2007; Pokrovski et al., 2008a, 2009b; this study). The formation of higher-order chloride species for Cu^I
647 and Ag^I, AgCl₃²⁻ (this study) and CuCl₃²⁻ (Brugger et al., 2007), is limited to low and moderate
648 temperatures (< 200-250°C) and high salt contents, and no tri- or tetra-chloride species have so far been
649 reported for monovalent Au^I (Pokrovski et al., 2009b). SUPCRT-derived databases (e.g., Sverjensky et
650 al., 1997; Parkhurst and Appelo, 1999) that use extrapolations from low-T data are likely to overestimate
651 the amount of higher-order Cl complexes both for Cu (Brugger et al., 2007) and Ag (this study). The
652 stability constants of the corresponding mono-, di- and tri-chloride complexes of Cu and Ag reported in
653 recent studies (Akinfiev and Zotov, 2001; Brugger et al., 2007; as well as Sverjensky et al., 1997 for

654 mono- and di-chloride species) are similar within the data scatter, implying a similar affinity of both
655 metals for the chloride ligand in aqueous solution over a wide T-range.

656 However, despite the large similarities in stoichiometry (amongst Cu, Ag, Au) and stability
657 (between Cu and Ag) of chloride complexes, this study revealed some differences in the molecular
658 structure of AgCl_2^- compared to CuCl_2^- and AuCl_2^- . The angular shape ($\angle\text{Cl-Ag-Cl} \sim 160^\circ$) and large Ag-
659 Cl distances ($R_{\text{AgCl}} \sim 2.38 \text{ \AA}$) of the Ag complex contrast with the quasi-linear geometry and much shorter
660 metal-Cl distances in its Au and Cu analogs, ($\angle\text{Cl-Cu-Cl} \sim 170\text{-}180^\circ$, $R_{\text{CuCl}} \sim 2.12\text{-}2.15 \text{ \AA}$, Fulton et al.,
661 2000; Brugger et al., 2007; $\angle\text{Cl-Au-Cl} \sim 180^\circ$, $R_{\text{AuCl}} \sim 2.27 \text{ \AA}$, Pokrovski et al., 2009b). The shortening of
662 metal-chloride distances from Ag to Au may be partly explained by relativistic contraction of the Au^+
663 radius (Pyykkö, 1988). We are not aware of the existence of solid compounds in which Ag is two-
664 coordinate by chlorides in a linear geometry; the available data show that Ag-Cl coordination geometries
665 range from 3 to 6-coordinate. More generally, in contrast with Cu and Au, Ag rarely form two-
666 coordinated complexes with other ligands in solids, preferring distorted penta-, tetra- or tri-coordinated
667 geometries (ICSD, 2010). This tendency is also seen in aqueous solution, with the tetra-coordinated
668 $\text{Ag}(\text{H}_2\text{O})_4^+$ (this study) compared with the linear $\text{Cu}(\text{H}_2\text{O})_2^+$ (Fulton et al., 2000). The higher Ag
669 coordination than that of Cu and Au results in a pronounced maximum for the metal-oxygen distances in
670 the row of the hydrated cations $\text{Cu}^+\text{-Ag}^+\text{-Au}^+$ ($R_{\text{Cu-H}_2\text{O}} \sim 1.9 \text{ \AA}$, Fulton et al., 2000; $R_{\text{Ag-H}_2\text{O}} \sim 2.3 \text{ \AA}$, Seward
671 et al., 1996, this study; $R_{\text{Au-H}_2\text{O}} \sim 2.0 \text{ \AA}$, Feller et al., 1999). The tendency of Ag to form higher
672 coordinated and less compact complexes than Cu and Au is also expressed in the angular shape and large
673 Ag-Cl distances in AgCl_2^- offering a less screened environment for Ag^+ and favoring outer-sphere
674 interactions with ions and solvent molecules in the fluid, compared to the more compact linear CuCl_2^- and
675 AuCl_2^- . These structural differences may partly be responsible for the fractionation of Ag vs Cu and Au in
676 brine-vapor-melt systems (section 5.1 below).

677 The molecular environment of metals such as Zn, Cd, Co, and Fe in saline hydrothermal solutions
678 appears to be different. Although all these divalent metals are also transported as chloride complexes in

679 the great majority of crustal fluids (Wood and Samson, 1998; Yardley, 2005; Pokrovski et al., 2008a;
680 Bazarkina et al., 2010), they form octahedral or tetrahedral entities containing both chloride and water in
681 the first coordination sphere of the metal cation, as shown by UV-visible and XAS measurements (Susak
682 and Crerar, 1985; Bazarkina et al., 2010; references therein). The octahedral-to-tetrahedral transition in
683 the metal coordination takes place with increasing both the temperature and the number of Cl ligands in
684 the dominant complex, so that low-order chloride species are octahedral (e.g., $\text{Zn}(\text{H}_2\text{O})_5\text{Cl}^+$, $\text{Fe}(\text{H}_2\text{O})_5\text{Cl}^+$,
685 $\text{Cd}(\text{H}_2\text{O})_5\text{Cl}^+$) and high-order tetrahedral (e.g., ZnCl_4^{2-} , FeCl_4^{2-} , $\text{CdCl}_3\text{H}_2\text{O}^-$). This may be explained
686 qualitatively by partial charge constraints on the Cl and H_2O ligands when increasing the number of Cl
687 atoms in the complex (Jolivet et al., 1994), and by the growth of thermal disorder with T favoring more
688 compact (and thus less coordinate) species of lower entropy (Brimhall and Crerar, 1987). However, the
689 major discrepancies in this picture concern the di-chloride complexes of these metals, in particular Zn and
690 Fe, which were believed to be dominant in high T geological fluids of low dielectric constant that favors
691 the stability of uncharged and weakly charged species (e.g., Brimhall and Crerar, 1987). First, it remains
692 unclear whether such di-chloride complexes are tetrahedral or octahedral (i.e., the only difference is by
693 two water molecules in the first shell of the metal) and whether they may exist in both coordinations.
694 Second, there exist large discrepancies between mineral solubility data, which systematically indicate the
695 dominant formation of di-chloride complexes in moderate-to-high saline fluids ($m_{\text{Cl}} > 0.1\text{m}$) at $T > 250$ -
696 300°C for both zinc and iron(II) (Ruaya and Seward, 1986; Bourcier and Barnes, 1987; Cygan et al.,
697 1994; Fein et al., 1992; Ohmoto et al., 1994; Yardley, 2005), and recent XAS measurements in Fe and Zn
698 chloride solutions, which report the predominance of double-charged tetra-chloride complexes, FeCl_4^{2-}
699 and ZnCl_4^{2-} , at similar conditions (e.g., Mayanovic et al., 1999; Testemale et al., 2009). Resolving these
700 discrepancies requires combined studies using new molecular modeling approaches (e.g., MD and
701 XANES modeling) and in situ spectroscopy, potentiometry, and solubility techniques. The impact of
702 these discrepancies on the interpretation of metal transport and deposition by geological fluids remains to
703 be understood.

704

705 **5. IMPLICATIONS FOR Cu-Ag-Au FRACTIONATION IN HYDROTHERMAL PROCESSES**

706

707 **5.1. Structural control: vapor-brine and fluid-melt partitioning**

708 The results of this study, together with the recent published work on Au and Cu aqueous speciation
709 and solubility, help to appreciate the impact of structural differences among dissolved metal species on
710 the behavior of Ag, Cu, and Au in natural hydrothermal-magmatic systems. These differences primarily
711 affect the partitioning of the metals between brine, melt, and vapor phases. The angular structure of the
712 Ag di-chloride complex, yielding a non-zero dipole moment likely favoring stronger interactions with
713 outer sphere Na, Cl, and H₂O as compared to its Cu and Au analogs, may account for the elevated affinity
714 of Ag for the hydrothermal brine phase. It explains the stronger partitioning of Ag than Cu or Au in favor
715 of the brine in vapor-brine and melt-brine systems as observed in natural fluid inclusions from
716 hydrothermal-magmatic deposits and laboratory experiments. For example vapor/brine and melt/brine
717 partition coefficients of Ag ($K = C_{\text{vapor}}/C_{\text{brine}}$, or $C_{\text{melt}}/C_{\text{brine}}$, where C is Ag concentration in the
718 corresponding phase) in water-salt sulfur-free laboratory systems at hydrothermal-magmatic conditions
719 are up a factor of 10 lower than those of Cu (Pokrovski et al., 2005a; Simon et al., 2006, 2008). Natural
720 data from coexisting low-to-moderate salinity fluid (< 1-3 m_{Cl}) and silicate melt inclusions from granitic
721 systems display similar differences ($K_{\text{fluid/melt}} \sim 1-10$ and $\sim 10-1,000$ for Ag and Cu, respectively, Zajacz et
722 al., 2008), which confirms the weaker Ag versus Cu affinity for the low saline fluid phase. By contrast,
723 Ag and Cu partitioning is similar between highly saline fluid and silicate melt inferred from the same type
724 of inclusions ($K_{\text{fluid/melt}} \sim 10-50$ for both Ag and Cu). In addition, $K_{\text{fluid/melt}}$ values of Ag systematically
725 increase in favor of the fluid with increasing chloride content, whereas those of Cu show no clear
726 correlation with m_{Cl} (Zajacz et al., 2008). Similar elevated Ag partition coefficients between 30 wt% salt
727 brine and silicate melt ($K_{\text{fluid/melt}} \sim 50$), comparable to those for Zn and Pb, were recently reported in
728 granitic pegmatites (Borisova et al., 2012).

729
730
731
732
733
734
735
736
737
738
739
740
741
742
743
744
745
746
747
748
749
750
751
752
753

5.2. Chemical speciation control: chloride versus sulfide

The differences in metal partitioning are further accentuated by the presence of reduced sulfur that further increases Cu (and Au) volatility compared with Ag. For example, vapor/brine partitioning coefficients ($K_{\text{vapor/brine}}$) of metals in S-rich (up to 1-2 wt% $\text{H}_2\text{S}+\text{SO}_2$ in the vapor phase) porphyry systems (e.g., Seo et al., 2009; Kouzmanov and Pokrovski, 2013; references therein) and laboratory experiments (Pokrovski et al., 2008a) increase in the order $\text{Fe} \approx \text{Zn} < \text{Ag} < \text{Cu} < \text{Au}$, attaining values of ~ 50 in favor of the vapor phase for Au due to the formation of volatile complexes with sulfur (H_2S and/or SO_2). The lowest volatility of base metals (typical $K_{\text{vapor/brine}}$ for Fe and Zn ~ 0.001 - 0.1 , Kouzmanov and Pokrovski, 2012) is a direct consequence of i) their weak affinity for reduced sulfur ligands (Wood and Samson, 1998) and ii) the large stability of their hydrated chloride complexes in the high-salinity aqueous solution (section 4.2). Both elevated absolute copper concentrations in some natural vapor-like inclusions from porphyry deposits (~ 1000 ppm) and the corresponding $K_{\text{vapor/brine}}$ values above 1 should now be regarded as post-entrapment modifications due to preferential diffusion of Cu from the external fluid into the S-rich inclusion as suggested by recent experiments (Lerchbaumer and Audetat, 2012), whereas Au and Ag are unlikely to be affected by this phenomenon. Thus, the majority of experimental studies show Cu vapor-brine partition coefficients to be between those of Ag and Au (see Kouzmanov and Pokrovski, 2013 for a recent review). The highest volatility of Au in the order above is consistent with the far larger stability of its known sulfide complexes compared to other metals and, in particular, the formation of neutral and weakly polar species with hydrogen sulfide (e.g., $\text{Au}(\text{H}_2\text{S})\text{HS}^0$, Pokrovski et al., 2009a), which are expected to be stable in the vapor phase of low density and dielectric constant. In contrast, the higher volatility of Cu than Ag in such S-rich systems is not consistent with the very similar stabilities and stoichiometries of their chloride and sulfide complexes in dense aqueous solution (see section 4.2). It may thus be hypothesized that structural differences exist between Ag and Cu species in both the low-density H_2S -rich vapor and saline liquid phase, which are fundamentally related to the tendency of Ag to form

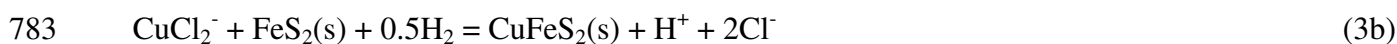
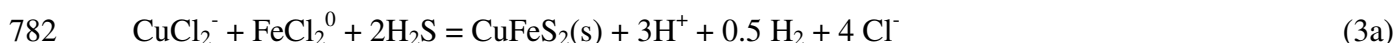
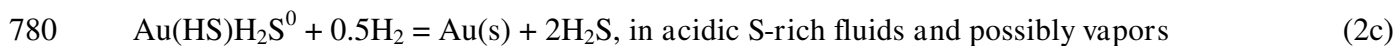
754 larger and higher-coordinated complexes than Cu. Thus, the contrasting affinity for chloride versus
 755 sulfide ligands of Ag, Au, and base metals, together with structural differences amongst complexes of the
 756 same ligand type, account for the volatility trends. These trends may explain the enrichment by Au and
 757 partly Cu, compared to Ag and base metals, of certain types of epithermal ore deposits regarded as being
 758 formed by ascending magmatic vapor (e.g., high sulfidation Cu-Au, Heinrich et al., 1999; Carlin-type Au
 759 deposits, Muntean et al., 2011; refs therein).

761 **5.3. Solid-phase control: mineral solubility**

762 If the structure and stability of dissolved metal complexes are the primary factors controlling the
 763 metal fractionation in fluid/melt and vapor/brine systems, in the presence of solid phases, another
 764 fundamental factor affecting the metal behavior during the formation of hydrothermal deposits is the
 765 identity and stability of the major metal-bearing minerals themselves. They are, respectively, chalcopyrite
 766 (CuFeS₂), argentite/acanthite (Ag₂S), and native gold (Au) for Cu, Ag, and Au in the great majority of
 767 deposits. Although Ag also forms complex sulfosalts with As, Sb and Cu, their solubility trends can be
 768 reasonably approximated by the Ag₂S component. In low-temperature deposits, silver and gold may also
 769 form alloys with Au contents as low as 40%, but this has a minor affect on Au solubility trends by
 770 lowering Au activity in the solid and solution by only a factor of 2 to 3, which is insignificant compared
 771 to the variations of several orders of magnitude in Au concentrations in natural hydrothermal fluids
 772 (Kouzmanov and Pokrovski, 2012). Thus CuFeS₂, Ag₂S, and Au may be used as model compounds for
 773 identifying the major trends in the behavior of these metals during fluid-rock interactions. Below we
 774 briefly summarize the main differences in the solubility patterns of these metals in hydrothermal systems.

775 The solubility controlling reactions for these metals in the majority of hydrothermal contexts are the
 776 following:





784 The differences in the major aqueous species and solid phases among these metals yield fundamentally
 785 different solubility trends versus pH, H₂S and salinity for Ag and Cu on one side and Au on the other. Fig.
 786 12 shows the solubility of all three minerals as a function of pH, H₂S and Cl in a typical hydrothermal
 787 fluid at 400°C and 0.5 kbar (i.e., conditions in the middle of the T-P range of their deposits formation),
 788 and as a function of temperature at 0.3-1.0 kbar, calculated using the stability constants available for these
 789 reactions from sources indicated in the figure caption. It can be seen that at a given T-P, the factors
 790 leading to the deposition of Au vs Ag and Cu are opposite. Gold precipitation requires: a) removing
 791 reduced sulfur from the fluid (e.g., via reaction with Fe-rich rocks, fluid boiling); b) acidifying the near-
 792 neutral fluid (e.g., SO₂ disproportionation into sulfuric acid and H₂S, common in porphyry systems); c)
 793 reducing the fluid (e.g., reaction with organic-rich sediments). In contrast, both Ag and Cu precipitation
 794 requires: a) removing chloride (e.g., dilution with meteoric waters), b) neutralizing the fluid (e.g., reaction
 795 with carbonate rocks, which is typical of skarns), c) oxidizing the fluid (e.g., mixing with meteoric waters,
 796 reaction with ferric-iron sediments). Note that addition of reduced sulfur into the system (e.g., via
 797 disproportionation of SO₂ into sulfide and sulfate in a cooling magmatic fluid or reaction with S-rich
 798 sedimentary rocks) decreases the solubility of silver in contrast to Au (Fig. 12d), but has no effect on the
 799 solubility of the CuFeS₂-FeS₂ assemblage (H₂S is not involved in reaction 3b). In addition, some of the
 800 factors listed above may operate in an opposite way (e.g., dilution with meteoric oxidizing waters will
 801 lower both Cl and H₂S concentrations, which have an opposite effect on the solubility of Ag and Cu-
 802 bearing sulfides, see reactions 1 and 3a,b), so that the final result on the mineral solubility will be an
 803 interplay between all these factors in a given natural case. The only common effect on all three elements
 804 is temperature whose decrease leads to a drop in solubility but of different amplitude depending of the
 805 metal (Fig. 12a).

806 The major differences in Au vs Ag solubility apparent in Fig. 12 account, at least partly, for the
807 Au/Ag ratios found in different types of deposits. For example, elevated Au/Ag ratios (typically 1-100)
808 and high Au fineness (i.e., Au fraction in Ag-Ag alloys) generally occur in Au-Te, Cu-Au epithermal,
809 skarn and gold orogenic deposits characterized by neutral-to-alkaline low-to-moderately saline fluids
810 (e.g., Morrison et al., 1991; Pal'yanova, 2008) having a high capacity to concentrate and transport gold
811 (Fig. 12b). Carlin-type Au and some Cu-Au high-sulfidation deposits are also characterized by elevated
812 Au/Ag ratios consistent with their likely formation by S-rich magmatic vapor phases carrying
813 preferentially Au as sulfide complexes (Pokrovski et al., 2008a; Muntean et al., 2011; references therein).
814 Lower Au/Ag ratios (~0.001-10) are typical for epithermal alunite and adularia Au-Ag deposits (Sillitoe
815 and Hedenquist, 2003; Pal'yanova, 2008; references therein) formed by acidic fluids of elevated salinity
816 (10-20 wt% NaCl) favorable for Ag solubility (see Fig. 12b,c).

817 Although it is more difficult to place Cu in this picture of solubility control because of its much
818 greater abundance than Ag and Au in most types of fluids, some qualitative trends in Cu vs Ag and Au
819 fractionation may still be identified in certain types of ore deposits. For example, despite large variations
820 of Cu/Au ratios in porphyry-style Cu-Au-Mo deposits (from 10^3 to 10^6), they roughly increase with depth
821 (Murakami et al., 2010). This was qualitatively interpreted by the more efficient precipitation of
822 chalcopyrite than gold from an ascending cooling magmatic fluid carrying Cu in the form of chloride
823 complexes, whereas Au remained in the fluid as soluble sulfide species (Murakami et al., 2010). Fig. 12a
824 shows CuFeS_2 , Ag_2S and Au solubility in a 10wt% salt fluid as a function of temperature at pressure
825 progressively decreasing from 1000 bar at 550°C to 300 bar below 300°C under redox and acidity
826 conditions buffered by silicate and Fe sulfide and oxide mineral assemblages typical of porphyry-style
827 deposits (e.g., Sillitoe, 2010; references therein). It can be seen that the slope of the CuFeS_2 solubility
828 curve is indeed significantly steeper than that of Au in the T range 300-500°C, in which major ore
829 deposition occurs in porphyry deposits. This temperature dependence of solubility, coupled with the 1,000
830 times higher amount of Cu compared to that of Au in the fluid, leads to massive Cu precipitation with

831 temperature drop. The solubility of Ag_2S at such conditions is comparable with that of CuFeS_2 , with
832 concentrations of 100's ppm Ag (Fig. 12). This is, however, typically 10 to 50 times higher than typical
833 abundances of Ag in natural moderate-salinity fluids and melts as inferred from inclusions (Kouzmanov
834 and Pokrovski, 2012; references therein). Most of saline high-T fluids are thus under-saturated with
835 respect of Ag-bearing solid phases. This explains the rarity of hydrothermal silver minerals at $T > 300$ -
836 350°C , and the fact that most silver resources are found in low-temperature epithermal deposits formed
837 below 300°C . This distinguishes Ag from Au and Cu that form hydrothermal deposits in a wide T range
838 from ~ 600 down to 150°C , and is thus a direct consequence of the solubility of their major minerals.

839 As a conclusion, the structure and stoichiometry of chloride complexes of Ag and accompanying
840 metals should be taken into account when interpreting metal fractionations in fluid-vapor and fluid-melt
841 systems. It seems to exert a lesser effect, however, on the metal behavior in mineral-fluid systems where
842 differences in the nature of the ligand in the dominant dissolved complexes (chloride for Ag, chloride and
843 possibly sulfide for Cu, and sulfide for Au), coupled with differences in the chemistry and solubility of
844 their principal minerals (sulfides for Cu and Ag, native metal for Au), largely control the metal transport
845 by crustal fluids and vapors and their precipitation as hydrothermal ores.

847 6. CONCLUDING REMARKS

848 This report is the first measurement, to the best of our knowledge, that uses in situ X-ray
849 absorption spectroscopy to determine the stability and structure of Ag(I) chloride-bearing complexes
850 in aqueous fluids pertinent to hydrothermal-magmatic systems. The combination of XANES and
851 EXAFS spectra analyses, molecular dynamics modeling of structures of Ag-Cl aqueous complexes,
852 and in situ solubility measurements of our study with thermodynamic analysis of published datasets
853 provide new constraints on the identity, structure, and stability of major Ag-Cl species operating in
854 natural hydrothermal fluids. The following major conclusions have been reached.

855 1) The silver di- and tri-chloride complexes, AgCl_2^- and AgCl_3^{2-} , are the major species forming in
856 moderate-temperature (200-300°C) aqueous solutions in a wide range of salinity (to at least 6m Cl,
857 corresponding to ~26 wt% NaCl equivalent). These species have an angular and triangular geometry,
858 respectively, with mean Ag-Cl distances of ~2.40 (AgCl_2^-) and 2.55 Å (AgCl_3^{2-}). The non-linear geometry
859 of AgCl_2^- revealed by MD and XANES modeling (angle Cl-Ag-Cl ~ 160°) is due to interactions with
860 surrounding water molecules and increasing dynamic disorder with temperature in aqueous solution. The
861 fraction of the tri-chloride species decreases with increasing temperature and decreasing chloride
862 concentration, so that AgCl_2^- becomes by far the major Ag-transporting complex at elevated temperatures
863 (> 350°C) in typical magmatic-hydrothermal fluids. Both species exhibit long-range interactions with the
864 surrounding water molecules and salt ions as revealed by MD simulations. The tetra-chloride complex,
865 AgCl_4^{3-} , suggested in previous work at low-temperatures (< 150°C), may be regarded as AgCl_2^- exhibiting
866 outer-sphere electrostatic interactions with two from four Cl⁻ ligands at distances > 3 Å. The coordination
867 environment of Ag in its dominant species in solution appears to be different from that of most Ag-
868 bearing solids, in which Ag has distorted coordination geometries with 3 to 6 Cl/O atoms, and from Cl-
869 free acidic solutions, in which the Ag^+ cation forms a distorted hydration sphere with 4 to 6 H₂O
870 molecules.

871 2) The species fractions derived from XAS and MD analyses, together with XAS-measured AgCl(s)
872 solubility, are in excellent agreement with thermodynamic predictions using the stability constants of
873 AgCl_2^- and AgCl_3^{2-} from Akinfiev and Zotov (2001) and Zotov et al. (1995), respectively, that are based
874 on extensive AgCl(s) solubility experiments. Our data also qualitatively agree with the pioneering
875 AgCl(s) solubility measurements of Seward (1976). In contrast, our results disagree with SUPCRT-based
876 datasets for Ag-Cl species (e.g., Sverjensky et al., 1997; Parkhurst and Angelo, 1999) derived by
877 extrapolation from low-temperature data, which predict large fractions of the high-order chloride species,
878 AgCl_3^{2-} and AgCl_4^{3-} , in high-temperature fluids. Thus, we recommend the thermodynamic set of Zotov's

879 group for chemical equilibrium calculations in Ag-bearing mineral-fluid systems above 200°C. A full set
880 of revised HKF parameters for silver chloride complexes will be presented in a future contribution.

881 3) Silver chloride complexes found in this work have longer Ag-Cl distances and stronger outer-
882 sphere interactions with the solvent and electrolytes than their Au and Cu counterparts. This may explain
883 the preferential partitioning of Ag into brine in brine-vapor and brine-melt magmatic-hydrothermal
884 systems compared with Cu and Au, as observed in natural melt and fluid inclusions and laboratory
885 experiments.

886 4) However, details of molecular structure of Ag, Cu, and Au complexes (geometry, inter-atomic
887 distances and solute-solvent interactions) matter much less in sulfur-rich hydrothermal environments and
888 most fluid-mineral systems where the contrasting affinity of these metals for sulfur ligands (with Au
889 forming far more stable complexes than Ag and Cu with reduced sulfur), coupled with the different
890 stability of their main solid phases (Ag sulfides, Cu-Fe sulfides, and native Au), largely controls the
891 transport and distribution of these metals by geological fluids and Ag/Au/Cu ratios in economic deposits.

892
893 Acknowledgements: This work was supported by CNRS grants from the French GDR Transmet, 3F (Fluides-
894 Failles-Flux), INSU-Actions Innovantes (CO2MET) programs, funds from the Laboratoire Européen Associé
895 Géochimie Environnementale (LEAGE), and the Agence Nationale de la Recherche (grant SOUMET - ANR 2011
896 Blanc SIMI 5-6 009), and by granted access to the HPC resources of CINES/IDRIS under the allocation 2011-
897 082309 from GENCI (Grand Equipement National de Calcul Intensif). We are grateful to the ESRF committee for
898 providing beam time and access to the synchrotron facility, G. Ciatto for his assistance at BM29 beamline, and D.
899 Testemale and Y. Joly for their help with XANES spectra modeling. Tatiana Pokrovski is acknowledged for her
900 assistance in the manuscript revision. Thoughtful reviews of T. Kashiwabara and two anonymous referees greatly
901 improved this article.

References

- 904 Akinfiev, N.N., Zotov, A.V., 1999. Thermodynamic description of equilibria in mixed fluids (H₂O-non-polar gas) over a wide
905 range of temperature (25-700°C) and pressure (1-5000 bars). *Geochim. Cosmochim. Acta* **63**, 2025-2041.
- 906 Akinfiev N.N. and Zotov A.V. (2001) Thermodynamic description of chloride, hydrosulphide, and hydroxide complexes of
907 Ag(I), Cu(I), and Au(I) at temperatures of 25-500°C and pressures of 1-2000 bar. *Geochem. Intern.* **39** (10), 990-1006.
- 908 Akinfiev N.N., Baranova N.N., Zotov A.V. and Tagirov B.R. (2008) Thermodynamic description of aqueous components in
909 the system Cu-Ag-Au-S-Se-O-H in the range of temperatures 0-600°C and pressures 1-3000 bars. In *Experimental*
910 *studies of endogenic processes* (eds. I. D. Ryabchikov, Yu. B. Shapovalov, E. G. Osadchii). Publishing Office of the
911 Institute of the Problems of Chemical Physics, Chernogolovka, Russia, pp. 184-203 (in Russian).
- 912 Armunanto R., Schwenk C.F., Rode B.M. (2003) Structure and dynamics of hydrated Ag(I): Ab initio quantum mechanical-
913 molecular mechanical molecular dynamics simulation. *J. Phys. Chem. A*, **107**, 3132-3138.
- 914 Anderko A. and Pitzer K.S. (1993) Equation-of-state representation of phase-equilibria and volumetric properties of the system
915 NaCl-H₂O above 573 K. *Geochim. Cosmochim. Acta* **57**, 1657-1680.
- 916 Audédat A., Günther D., and Heinrich C.A. (2000) Causes for large-scale metal zonation around mineralized plutons: Fluid
917 inclusion LA-ICP-MS evidence from the Mole Granite, Australia. *Econ. Geol.* **95**, 1563-1581.
- 918 Bakker R.J. (2003) Package FLUIDS 1. Computer programs for analysis of fluid inclusion data and for modelling bulk fluid
919 properties. *Chem. Geol.* **194**, 3-23.
- 920 Bazarkina E.F., Pokrovski G.S., Zotov A.V., Hazemann J-L. (2010) Structure and stability of cadmium chloride complexes in
921 hydrothermal fluids. *Chem. Geol.* **276**, 1-17.
- 922 Becke A. (1988) Density-functional exchange-energy approximation with correct asymptotic behavior. *Phys. Rev.A* **38**, 3098-
923 3100.
- 924 Bernasconi L., Blumberger J., Sprik M., Vuilleumier R. (2004) Density functional calculation of the electronic absorption
925 spectrum of Cu⁺ and Ag⁺ aqua ions. *J. Chem. Phys.* **121**, 11885-11899.
- 926 Berry A.J., Harris A.C., Kamenetsky V.S., Newville M., Sutton S.R. (2009) The speciation of copper in natural fluid inclusions
927 at temperatures up to 700°C. *Chem. Geol.* **259**, 1-6.
- 928 Borisova A.Y., Thomas R., Salvi S., Candaudap F., Lanzasova A., Chmieleff J. (2012) Tin and associated metal and metalloid
929 geochemistry by femtosecond LA-ICP-QMS microanalysis of pegmatite-leucogranite melt and fluid inclusions: new
930 evidence from melt-melt-fluid immiscibility. *Miner. Mag.* **76**, 91-133.
- 931 Bourcier W. L., Barnes H. L. (1987) Ore solution chemistry-VII. Stabilities of chloride and bisulfide complexes of zinc to
932 350°C. *Econ. Geol.* **82**, 1839-1863.
- 933 Brimhall G.H. and Crerar D.A. (1987) Ore fluids: magmatic to supergene. *Rev. Miner.* **17**, 235-321.
- 934 Brugger J., Etschmann B., Liu W., Testemale D., Hazemann J.L., Emerich H., Van Beek W., Proux O. (2007). An XAS study
935 of the structure and thermodynamics of Cu(I) chloride complexes in brines up to high temperature (400°C, 600 bar).
936 *Geochim. Cosmochim. Acta* **71**, 4920-4941.
- 937 Crerar D., Wood S. and Brantley S. (1985) Chemical controls on solubility of ore-forming minerals in hydrothermal solutions.
938 *Can. Miner.* **23**, 333-352.
- 939 Cygan G. L., Hemley J. J., D'Angelo W. M. (1994). An experimental study of zinc chloride speciation from 300 to 600°C and
940 0.5-2.0 kbar in buffered hydrothermal solutions. *Geochim. Cosmochim. Acta* **58**, 4841-4855.
- 941 Dang L.X., Schenter G.K., Glezakou V.A. and Fulton J.L. (2006) Molecular simulation analysis and X-ray absorption
942 measurement of Ca²⁺, K⁺ and Cl⁻ ions in solution, *J. Phys. Chem. B* **110**, 23644-23654.
- 943 D'Angelo P., Migliorati V., Mancini G. and Chellemi G. (2008) A coupled molecular dynamics and XANES data analysis
944 investigation of aqueous cadmium(II). *J. Phys. Chem. A* **112**, 11833-11841.
- 945 Etschmann B.E., Liu W., Testemale D., Müller H., Rae N.A., Proux O., Hazemann J.L., Brugger J. (2010) An in situ XAS
946 study of copper(I) transport as hydrosulfide complexes in hydrothermal solutions (25-592°C, 180-600 bar): Speciation
947 and solubility in vapor and liquid phases. *Geochim. Cosmochim. Acta* **74**, 4723-4739.
- 948 Fein J.B., Hemley J.J., d'Angelo W.M., Komninou A., Sverjensky D.A. (1992) Experimental study of iron-chloride
949 complexing in hydrothermal fluids. *Geochim. Cosmochim. Acta* **56**, 3179-3190.
- 950 Feller D., Glendening E. D. and Jong, W. A. (1999) Structures and binding enthalpies of M⁺(H₂O)_n clusters, M=Cu, Ag, Au. *J.*
951 *Chem. Phys.* **110**, 1475-1491.
- 952 Ferlat G., San Miguel A., Jal J. F., Soetens J. C., Bopp Ph. A., Hazemann J. L., Testemale T., Daniel I. (2002) The quest for ion
953 pairing in supercritical aqueous electrolytes. *J. Mol. Liq.* **101**, 127-136.
- 954 Ferlat G., Soetens J. C., San Miguel A., Bopp Ph. A. (2005) Combining extended x-ray absorption fine structure with
955 numerical simulations for disordered systems. *J. Phys. Condens. Matter* **17**, S145-S157.

- 956 Filipponi A., Borowski M., Bowron D.T., Ansell S., De Panfilis S., Di Cicco A., Itie J.-P. (2000) An experimental station for
957 advanced research on condensed matter under extreme conditions at the European synchrotron radiation facility - BM29
958 beamline. *Rev. Sci. Instruments* **71**, 2422-2432.
- 959 Fulton J.L., Hoffmann M.M., Darab J.G. (2000) An X-ray absorption fine structure study of copper(I) chloride coordination
960 structure in water up to 325°C. *Chem. Phys. Lett.* **330**, 300-308.
- 961 Fulton J.L., Kathmann S.M., Schenter G.K., Balasubramanian M. (2009) Hydrated structure of Ag(I) ion from symmetry-
962 dependent, K- and L-edge XAFS multiple scattering and molecular dynamics simulations. *J. Phys. Chem A* **113**, 13976-
963 13984.
- 964 Gammons C.H. (1995) Experimental investigations of hydrothermal geochemistry of Pt and Pd. IV. The stoichiometry of
965 Pt(IV) and Pd(II) chloride complexes at 100 to 300°C. *Geochim. Cosmochim. Acta* **59**, 1655-1668.
- 966 Gammons C.H., Williams-Jones A.E. (1995) The solubility of Au-Ag alloy + AgCl in HCl/NaCl solutions at 300°C: New data
967 on the stability of Au(I) chloride complexes in hydrothermal fluids. *Geochim. Cosmochim. Acta* **59**, 3453-3468.
- 968 Gammons C.H. and Seward T.M. (1996) Stability of manganese(II) chloride complexes from 25 to 300°C. *Geochim.*
969 *Cosmochim. Acta* **60**, 4295-4311.
- 970 Gammons C.H., Yu Y. (2007) The stability of aqueous silver bromide and iodide complexes at 25–300°C: Experiments, theory
971 and geologic applications. *Chem. Geol.* **137**, 155-173.
- 972 Gammons C.H., Wood S.A., Williams-Jones A.E. (1996) The aqueous geochemistry of rare earth elements and yttrium: VI.
973 Stability of neodymium chloride complexes from 25 to 300°C. *Geochim. Cosmochim. Acta* **60**, 4615-4630.
- 974 Gibbons C.S., Trotter J. (1971) Crystal structure of exo-Tricyclo[3,2,1,0^{2,4}]oct-6-ene-silver nitrate, and a refinement of the
975 silver nitrate structure. *J. Chem. Soc. A*, 2058-2062.
- 976 Godinho S.S.M.C., Cabral do Couto P., Costa Cabral B.J. (2005) Polarization effects and charge separation in AgCl-water
977 clusters. *J. Chem. Phys.* **122**, 044316, 1-14.
- 978 Goedecker S., Teter M., and Hutter J. (1996). Separable dual-space gaussian pseudopotentials. *Physical Review B* **54**, 1703–
979 1710.
- 980 Grimme S. (2006). Semiempirical GGA-type density functional constructed with a long-range dispersion correction. *J.*
981 *Comput. Chem.* **27**, 1787.
- 982 Hartwigsen C., Goedecker S., and Hutter J. (1998). Relativistic separable dual-space gaussian pseudopotentials from H to Rn.
983 *Physical Review B* **58**, 3641–3662.
- 984 Heinrich, C.A., Günther, D., Audédat, A., Ulrich, T., Frischknecht, R, 1999. Metal fractionation between magmatic brine and
985 vapour, and the link between porphyry-style and epithermal Cu-Au deposits. *Geology* **27**, 755-758.
- 986 Hull S., Keen D. A. (1999) Pressure-induced phase transitions in AgCl, AgBr, and AgI. *Phys. Rev.* **B 59**, 750-761.
- 987 ICSD (2010) Inorganic Crystal Structure Database, FIZ Karlsruhe, <http://www.fiz-karlsruhe.de/icsd.html>
- 988 Inui M., Takeda S., Shirakawa Y., Tamaki S., Waseda Y., Yamaguchi Y. (1991) Structural study of molten silver halides by
989 neutron diffraction. *J. Phys. Soc. Japan* **60**, 3025-3031.
- 990 Johnson J.W., Oelkers E.H. and Helgeson H.C. (1992) SUPCRT92: A software package for calculating the standard molal
991 thermodynamic properties of minerals, gases, aqueous species, and reactions from 1 to 5000 bar and 0 to 1000°C.
992 *Computers & Geosci.* **18**, 899-947; <http://geopig.asu.edu/index.html#>.
- 993 Jolivet J-P., Henry M., Livage J. (1994) *De la Solution à l'Oxide*. InterEditions & CNRS Editions, 249p.
- 994 Joly Y. (2001) X-ray absorption near-edge structure calculations beyond the muffin tin approximation. *Phys. Rev.* **B 63**,
995 125120.
- 996 Kawakita Y., Enosaki T., Takeda S., Maruyama K. (2007) Structural study of molten Ag halides and molten AgCl-AgI mixture.
997 *J. Non-Cryst. Solids* **535**, 3035-3039.
- 998 Kelly S.D., Hesterberg D., Ravel B. (2008) Analysis of soils and minerals using X-ray absorption spectroscopy. *Methods of Soil*
999 *Analysis. Part 5. Mineralogical Methods*, p. 387-463, Soil Sci. Soc. Am., Madison, USA.
- 1000 Kouzmanov K., Pokrovski G.S. (2013) Hydrothermal controls on metal distribution in porphyry systems. *Society of Economic*
1001 *Geologists Special Publication*, accepted.
- 1002 Krack M. (2005). Pseudopotentials for H to Kr optimized for gradient-corrected exchange- correlation functionals. *Theor.*
1003 *Chem. Acc.* **114**, 145-152.
- 1004 Lee C., Yang W., and Parr R. (1988). Development of the colle-salvetti correlation-energy formula into a functional of the
1005 electron-density. *Phys. Rev.B* **37**, 785-789.
- 1006 Lerchbaumer L., Audédat A. (2012) High Cu concentrations in vapor-type fluid inclusions: An artifact? *Geochim. Cosmochim.*
1007 *Acta* **88**, 255-274.

- 1008 Lippert G., Hutter J., and Parrinello M. (1997). A hybrid gaussian and plane wave density functional scheme. *Molecular*
1009 *Physics* **92**, 477-487.
- 1010 Liu X., Lu X., Wang R., Zhou H. (2012). Silver speciation in chloride-containing hydrothermal solutions from first principles
1011 molecular dynamics simulations. *Chem. Geol.* **294-295**, 103-112.
- 1012 Malinowski E.R. (1991) *Factor Analysis in Chemistry*. 2nd Edition, Wiley.
- 1013 Martell A.E., Smith R.M., Motekaitis R.J. (2004) *Critical: Critically Selected Stability Constants of Metal Complexes*
1014 *Database*. Version 8.0, NIST., Texas A & M University.
- 1015 Martinez J.M, Pappalardo R.R., Sanchez-Marcos E. (1997) Study of the Ag⁺ hydration by means of a semicontinuum quantum-
1016 chemical solvation model. *J. Phys. Chem. A*, **101**, 4444-4448.
- 1017 Marzari N., Mostofi A.A., Yates J.R., Souza I., Vanderbilt D. (2012) Maximally localized Wannier functions: Theory and
1018 applications. *Rev. Mod. Phys.* **84**, 1419-1475.
- 1019 Mayanovic R.A., Anderson A.J., Bassett W.A., Chou I.-M. (1999). XAFS measurements on zinc chloride aqueous solutions
1020 from ambient to supercritical conditions using the diamond anvil cell. *J. Synchrotron Rad.* **6**, 195-197.
- 1021 Munoz, M., Argoul, P., Farges F., 2003. Continuous cauchy wavelet transform analyses of EXAFS spectra: a qualitative
1022 approach. *Amer. Mineral.* **88**, 694-700.
- 1023 Manteau J.L., Cline J.S., Simon A.C., Longo A.A. (2011) Marmatic-hydrothermal origin of Nevada's Carlin-type gold
1024 deposits. *Nature Geoscience* **4**, 122-127.
- 1025 Morrison G.W., Rose W.J., Jaireth S. (1991) Geological and geochemical controls on the silver content (fineness) of gold-
1026 silver deposits. *Ore Geol. Rev.* **6**, 333-364.
- 1027 Murakami H., Seo J.H., Heinrich C.A. (2010) The relation between Cu/Au ratio and formation depth of porphyry-style Cu-
1028 Au±Mo deposits. *Miner. Deposita* **45**, 11-21.
- 1029 Newville M. (2001) IFEFFIT: interactive XAFS analysis and FEFF fitting. *J. Synchrotron Rad.* **8**, 322-324.
- 1030 Nosé, S. (1984a). A molecular-dynamics method for simulations in the canonical ensemble. *Mol. Phys.* **52**, 255-268.
- 1031 Nosé, S. (1984b). A unified formulation of the constant temperature molecular-dynamics methods. *J. Chem. Phys.* **81**, 511-
1032 519.
- 1033 Ohmoto H., Hayashi K-I., Kajisa Y. (1994) Experimental study of the solubilities of pyrite in NaCl-bearing aqueous solutions
1034 at 250-350°C. *Geochim. Cosmochim. Acta* **58**, 2169-2185.
- 1035 Pal'yanova G. (2008) Physicochemical modeling of the coupled behavior of gold and silver in hydrothermal processes: Gold
1036 fineness, Au/Ag ratios and their possible implications. *Chem. Geol.* **255**, 399-413.
- 1037 Parkhurst, D.L., Appelo, C.A.J., 1999. User's guide to PHREEQC (version 2) - a computer program for speciation, reaction-
1038 path, 1D-transport, and inverse geochemical calculations. US Geol. Surv. Water Resour. Inv. Rep. 99-4259, 312p.
- 1039 Persson I., Nilsson K.B. (2006) Coordination chemistry of the solvated silver(I) ion in thye oxygen donor solvents water,
1040 dimethyl sulfoxide, and N,N'-dimethylpropyleneurea. *Inorg. Chem.* **45**, 7428-7434.
- 1041 Pokrovski G.S., Roux J. and Harrichoury J.-C. (2005a). Fluid density control on vapor-liquid partitioning of metals in
1042 hydrothermal systems. *Geology* **33**, 657-660.
- 1043 Pokrovski G.S., Roux J., Hazemann J.-L. and Testemale D. (2005b) An X-ray absorption spectroscopy study of argutite
1044 solubility and germanium aqueous speciation in hydrothermal fluids to 500°C and 400 bar. *Chem. Geol.* **217**, 127-145.
- 1045 Pokrovski G.S., Borisova A.Yu., Roux J., Hazemann J.-L., Petdang A., Tella M. and Testemale D. (2006). Antimony
1046 speciation in saline hydrothermal fluids: A combined X-ray absorption fine structure and solubility study. *Geochim.*
1047 *Cosmochim Acta* **70**, 4196-4214.
- 1048 Pokrovski G.S., Borisova A.Yu. and Harrichoury J.-C. (2008a). The effect of sulfur on vapor-liquid fractionation of metals in
1049 hydrothermal systems. *Earth Planet. Sci. Lett.* **266**, 345-362.
- 1050 Pokrovski G.S., Roux J., Hazemann J.-L., Borisova A.Yu., Gonchar A.A. and Lemeshko M.P. (2008b) In situ X-ray absorption
1051 spectroscopy measurement of vapor-brine fractionation of antimony at hydrothermal conditions. *Min. Mag.* **72**, 667-
1052 681.
- 1053 Pokrovski G.S., Tagirov B.R., Schott J., Hazemann J.-L., Proux O. (2009a). A new view on gold speciation in sulfur-bearing
1054 hydrothermal fluids from in situ X-ray absorption spectroscopy and quantum-chemical modeling. *Geochim.*
1055 *Cosmochim. Acta* **73**, 5406-5427.
- 1056 Pokrovski G.S., Tagirov B.R., Schott J., Bazarkina E.F., Hazemann J.-L. and Proux O. (2009b) An in situ X-ray absorption
1057 spectroscopy study of gold-chloride complexing in hydrothermal fluids. *Chem. Geol.* **259**, 17-29.
- 1058 Pyykkö P. (1988) Relativistic effects in structural chemistry. *Chem. Rev.* **88**, 563-594.
- 1059 Ravel B. and Newville M. (2005) ATHENA, ARTEMIS, HEPHAESTUS: data analysis for X-ray absorption spectroscopy
1060 using IFEFFIT. *J. Synchrotron Rad.* **12**, 537-541.

- 1061 Robie R.A., Hemingway B.S. (1995) Thermodynamic Properties of Minerals and Related Substances at 298.15 K and 1 bar
1062 (10^5 pascals) pressure and at high temperatures. U. S. Geol. Surv. Bull. **2131**, 461p.
- 1063 Rossberg A., Reich T., Bernhard G. (2003) Complexation of uranium(VI) with protocatechuic acid – application of iterative
1064 transformation factor analysis to EXAFS spectroscopy. Anal. Bioanal. Chem. **376**, 631-638.
- 1065 Ruaya J.R. and Seward T.M. (1986) The stability of chloro-zinc (II) complexes in hydrothermal solutions up to 350°C.
1066 Geochim. Cosmochim. Acta **50**, 651-661.
- 1067 Ruaya J.R. and Seward T.M. (1987) The ion-pair constant and other thermodynamic properties of HCl up to 350°C. Geochim.
1068 Cosmochim. Acta **51**, 121-130.
- 1069 Rudnick, R.L., Gao, S., 2003. Composition of the Continental Crust. In: Holland, H.D., Turekian, K.K. (Eds.), Treatise on
1070 Geochemistry, Elsevier, Amsterdam.
- 1071 Sandström M., Neilson G.W., Johansson G., Yamaguchi T. (1985) Ag^+ hydration in perchlorate solution. J. Phys. C: Solid
1072 State Phys. **18**, L1115-L1121.
- 1073 Sayers D.E. (2000) Report of the International XAFS Society Standards and Criteria Committee. http://www.i-x-s.org/OLD/subcommittee_reports/sc/.
- 1074
- 1075 Seward T.M. (1976) The stability of chloride complexes of silver in hydrothermal solutions up to 350°C. Geochim.
1076 Cosmochim. Acta **40**, 1329-1341.
- 1077 Seward T.M., Henderson C.M.B., Charnock J.M., Dobson B.R. (1996) An X-ray absorption (EXAFS) spectroscopic study of
1078 aquated Ag^+ in hydrothermal solutions to 350°C. Geochim. Cosmochim. Acta **60**, 2273-2282.
- 1079 Sherman D.M. (2010) Metal complexation and ion association in hydrothermal fluids: insights from quantum chemistry and
1080 molecular dynamics. Geofluids **10**, 41-57.
- 1081 Shvarov Y.S. (2008) HCh: New potentialities for the thermodynamic simulation of geochemical systems offered by windows.
1082 Geochem. Intl. **46**, 834-839; <http://www.geol.msu.ru/deps/geochems/soft/index.html/>
- 1083 Skipper N.T., Neilson G.W. (1989) X-ray and neutron diffraction studies on concentrated aqueous solutions of sodium nitrate
1084 and silver nitrate. J. Phys.: Condens. Matter **1**, 4141-4154.
- 1085 Sillitoe R.H. (2010) Porphyry copper systems. Econ. Geol. **105**, 3-41.
- 1086 Sillitoe R.H., Hedenquist J.W. (2003) Linkages between volcanotectonic settings, ore-fluid compositions, and epithermal
1087 precious metal deposits. Soc. Econ. Geol. Spec. Pub. **10**, 315-343.
- 1088 Silvestrelli P.L., Parrinello M. (1999) Water molecule dipole in the gas and in the liquid phase. Phys. Rev. Lett. **82**, 3308-3311.
- 1089 Simon A.C., Pettke T., Candela P.A., Piccoli P.M., Heinrich C.A. (2006) Copper partitioning in a melt–vapor–brine–
1090 magnetite–pyrrhotite assemblage. Geochim. Cosmochim. Acta **70**, 5583-5600.
- 1091 Simon A.C., Pettke T., Candela P.A., Piccoli P.M. (2008) The partitioning behavior of silver in a vapor–brine–rhyolite melt
1092 assemblage. Geochim. Cosmochim. Acta **72**, 1638-1659.
- 1093 Seo J.H., Guillong M., Heinrich C.A. (2009) The role of sulfur in the formation of magmatic-hydrothermal copper-gold
1094 deposits. Earth Planet. Sci. Lett. **282**, 323-328.
- 1095 Sprik M., Hutter J., Parrinello M., (1996) Ab initio molecular dynamics simulation of liquid water: Comparison of three
1096 gradient-corrected density functionals. J. Chem. Phys. **105**, 1142-1152.
- 1097 Stefánsson A., Seward T.M. (2003). Experimental determination of the stability and stoichiometry of sulphide complexes of
1098 silver(I) in hydrothermal solutions to 400°C. Geochim. Cosmochim. Acta **67**, 1395-1413.
- 1099 Susak N.J., Crerar D.A. (1985) Spectra and coordination changes of transition metals in hydrothermal solutions: Implication
1100 for ore genesis. Geochim. Cosmochim. Acta **49**, 555-564.
- 1101 Sverjensky D.A., Shock E.L. and Helgeson H.C. (1997) Prediction of the thermodynamic properties of aqueous metal
1102 complexes to 1000°C and 5 kb. Geochim. Cosmochim. Acta **61**, 1359-1412.
- 1103 Tanger J.C., Helgeson H.C. (1988) Calculation of the thermodynamic and transport properties of aqueous species at high
1104 pressures and temperatures: Revised equations of state for the standard partial molal properties of ions and
1105 electrolytes. Amer. J. Sci. **288**, 19-98.
- 1106 Tagirov, B.R., Zotov, A.V., Akiniev, N.N., 1997. Experimental study of the dissociation of HCl from 350 to 500°C and from
1107 500 to 2500 bar. Thermodynamic properties of HCl^0 (aq). Geochim. Cosmochim. Acta **61**, 4267-4280.
- 1108 Testemale D., Hazemann J.-L., Pokrovski G.S., Joly Y., Roux J., Argoud R. and Geaymond O. (2004) Structural and electronic
1109 evolution of the $\text{As}(\text{OH})_3$ molecule in high temperature aqueous solutions: An x-ray absorption investigation. J. Chem.
1110 Phys. **121**, 8973-8982.
- 1111 Testemale D., Argoud R., Geaymond O. and Hazemann J.-L. (2005). High pressure/high temperature cell for x-ray absorption
1112 and scattering techniques. Rev. Sci. Instrum. **76**, 043905-043909.

- 1113 Testemale D., Brugger J., Liu W., Etschmann B., Hazemann J.-L. (2009) In-situ X-ray absorption study of iron(II) speciation in
1114 brines up to supercritical conditions. *Chem. Geol.* **264**, 295-310.
- 1115 Texter J., Hastreiter J.J., Hall J.L. (1983) Spectroscopic confirmation of the tetrahedral geometry of $\text{Ag}(\text{H}_2\text{O})_4^+$. *J. Phys. Chem.*
1116 **87**, 4690-4693.
- 1117 Ulrich, T., Günther, D., Heinrich, C.A., 1999. Gold concentrations of magmatic brines and the metal budget of porphyry
1118 copper deposits. *Nature* **399**, 676-679.
- 1119 VandeVondele J. and Hutter J. (2003). An efficient orbital transformation method for electronic structure calculations. *J.*
1120 *Chem. Phys.* **118**, 4365–4369.
- 1121 VandeVondele J., Krack M., Mohamed F., Parrinello M., Chassaing T., and Hutter J. (2005a). Quickstep: Fast and accurate
1122 density functional calculations using a mixed gaussian and plane waves approach. *Comput. Phys. Comm.* **167**, 103–128.
- 1123 VandeVondele J., Mohamed F., Krack M., Hutter J., Sprik M., and Parrinello, M. (2005b). The influence of temperature and
1124 density functional models in ab initio molecular dynamics simulation of liquid water. *J. Chem. Phys.* **122**, 014515.
- 1125 VandeVondele J. and Hutter J. (2007). Gaussian basis sets for accurate calculations on molecular systems in gas and condensed
1126 phases. *J. Chem. Phys.* **127**, 114105.
- 1127 Webster J.G. (1986) The solubility of gold and silver in the system Au-Ag-S-O₂-H₂O at 25°C and 1 atm. *Geochim.*
1128 *Cosmochim. Acta* **50**, 1837-1845.
- 1129 Williams-Jones A.E. and Seward T.M. (1989) The stability of calcium chloride ion pairs in aqueous solutions at temperatures
1130 between 100 and 360°C. *Geochim. Cosmochim. Acta* **53**, 313-318.
- 1131 Wood S., Crerar D.A. and Borcsik M.P. (1987) Solubility of the assemblage pyrite-pyrrhotite-magnetite-sphalerite-galena-
1132 gold-stibnite-bismuthinite-argentite-molybdenite in H₂O-NaCl-CO₂ solutions from 200 to 350°C. *Econ. Geol.* **82**, 1864-
1133 1887.
- 1134 Wood S.A., Samson I.M. (1998) Solubility of ore minerals and complexation of ore metals in hydrothermal solutions. *Rev.*
1135 *Econ. Geol.* **10**, 33-77.
- 1136 Yamaguchi T., Johansson G., Holmberg B., Maeda M., Ohtaki H. (1984a) The coordination and complex formation of silver(I)
1137 in aqueous perchlorate, nitrate, and iodide solutions. *Acta Chem. Scand.* **38A**, 437-451.
- 1138 Yamaguchi T., Lindquist O., Boyce J.B., Claesson T. (1984b) Determination of the hydration structure of silver ions in aqueous
1139 silver perchlorate and nitrate solutions from EXAFS using synchrotron radiation. *Acta Chem. Scand.* **38A**, 423-428.
- 1140 Yardley B.W. (2005) Metal concentrations in crustal fluids and their relationship to ore formation. *Econ. Geol.* **100**, 613-632.
- 1141 Zabinsky S.I., Rehr J.J., Ankudinov A., Albers R.S., Eller M.J. (1995) Multiple scattering calculations of X-ray absorption
1142 spectra. *Phys. Rev. B* **52**, 2995-3009.
- 1143 Zajacz Z., Halter W.E., Pettke T., Guillong M. (2008) Determination of fluid/melt partition coefficients by LA-ICPMS analysis
1144 of co-existing fluid and silicate melt inclusions: Controls on element partitioning. *Geochim. Cosmochim. Acta* **72**, 2169-
1145 2197.
- 1146 Zajacz Z., Seo J.H., Candela P.A., Piccoli P.M., Tossell J.A. (2011) The solubility of copper in high-temperature magmatic
1147 vapors: A quest for the significance of various chloride and sulfide complexes. *Geochim. Cosmochim. Acta* **75**, 2811-
1148 2827.
- 1149 Zotov A.V., Kudrin A.V., Levin K.A., Shikina N.D., and Var'yash L.N. (1995) Experimental studies of the solubility and
1150 complexing of selected ore elements (Au, Ag, Cu, Mo, As, Sb, Hg) in aqueous solutions. in: Shmulovich, K.I., Yardley,
1151 B.W.D., Gonchar, G.G. (Eds.), *Fluids in the Crust. Equilibrium and Transport Properties*, Chapman & Hall, London,
1152 pp. 95-138.
- 1153
- 1154

Table 1. Silver dissolved concentrations derived from the absorption edge step ^(a), and Ag(I) local structure derived from EXAFS spectra at Ag K-edge ^(b) of nitrate and chloride aqueous solutions investigated in this study.

T, °C	P, bar	m_{Ag} , mol/kg H ₂ O	atom	N, atoms	R, Å	σ^2 , Å ²	c_3 , Å ³	\mathcal{R} - factor
# 1: 0m total Cl, 0.21m AgNO₃-0.10m HNO₃-0.10m H₂O₂								
30	600	0.21±0.01	O	6.0	2.34	0.020	< 0.0003	0.003
100	600	0.21±0.02	O	5.5	2.32	0.020	< 0.0003	0.006
200	630	0.21±0.02	O	4.8	2.30	0.020	< 0.0003	0.010
				error	±1.5	±0.02	±0.005	±0.0003
# 6: 0.70m total Cl, 0.17m AgCl-0.42m NaCl-0.11m HCl-0.06m H₂O₂								
200	600	0.0074±0.0005	Cl	nd	nd	nd	nd	nd
300	600	0.049±0.003	Cl	1.8	2.38	0.005	0.0007	0.011
400	750	0.14±0.12	Cl	1.9	2.38	0.007	0.0005	0.010
450	750	0.11±0.08	Cl	1.9	2.37	0.007	0.0005	0.008
# 2-4: 2.6m total Cl, 0.18m AgCl-2.34m NaCl-0.12m HCl-0.06m H₂O₂								
200	600	0.047±0.003	Cl	2.1	2.47	0.009	0.0012	0.008
300	630	0.20±0.15	Cl	1.9	2.43	0.009	0.0009	0.009
400	600	0.15±0.13	Cl	1.9	2.40	0.008	0.0005	0.007
# 5: 5.9m total Cl, 0.30m AgCl-5.51m NaCl-0.14m HCl-0.07m H₂O₂								
200	600	0.16±0.02	Cl	2.5	2.49	0.012	0.0008	0.015
300	620	0.33±0.03	Cl	2.1	2.47	0.011	0.0012	0.009
400	630	0.29±0.03	Cl	1.9	2.44	0.010	0.0010	0.009
450	640	0.28±0.03	Cl	1.8	2.42	0.010	0.0007	0.010
				error	±0.2	±0.01	±0.003	±0.0004

(a) Dissolved Ag concentrations were determined from the amplitude of the absorption edge height of transmission spectra ($\Delta\mu$) based on the classical X-ray absorption relation (see for details Pokrovski et al., 2005a, 2006, 2009a,b; Testemale et al., 2005): $C_{\text{Ag}} = \Delta\mu / (\Delta\sigma_{\text{Ag}} \times M_{\text{Ag}} \times l \times d_{\text{fluid}})$, where C_{Ag} is Ag aqueous concentration (mol kg⁻¹ of fluid), $\Delta\sigma_{\text{Ag}}$ is the change of the total absorption cross-section of Ag over its K-edge (45.865 cm² g⁻¹), l is the optical path length inside the cell (0.40 cm) which remains constant through the experiment, M_{Ag} is Ag atomic weight (0.1079 kg mol⁻¹), and d_{fluid} is the density of the aqueous solution (g cm⁻³) at given T and P, estimated using the densities of NaCl-H₂O fluids (Bakker, 2003), and assuming that AgCl/HCl/H₂O₂ solutes in water yield the same contribution to the fluid density as the equivalent weight concentration of NaCl. Uncertainties on Ag concentration stem from those of the determination of $\Delta\mu$, l and d_{fluid} (see Pokrovski et al., 2005a, 2009a for details), and minor losses from solution due to AgCl_(s) precipitation. Values of m_{Ag} in italic show significant change with time owing to precipitation of AgCl in the cell colder zones; they were not considered in the solubility analyses.

(b) R = Ag-O/Cl mean distance, N = Ag coordination number, σ^2 = squared Debye-Waller factor (relative to $\sigma^2 = 0$ adopted in the calculation of reference amplitude and phase functions by FEFF); c_3 = third-order cumulant accounting for weak anharmonicity in the distance distribution; \mathcal{R} -factor defines goodness of the total fit in R-space, which is a fractional misfit between the data and model: $\mathcal{R} = \sum(\text{data} - \text{model})^2 / \sum \text{data}^2$. For all samples the fitted R-ranges are 1.1-2.8 Å (not corrected for phase shift), and k-ranges are 2.5-10.0 Å⁻¹ and 3.0-11.8 Å⁻¹ for nitrate and chloride solutions, respectively (except exp #6 at 300°C, which was recorded to 8 Å⁻¹). The value of Δe , which is a non-structural parameter accounting for phase shift between experimental spectrum and FEFF calculation, is 3.5±0.5 eV for all spectra. The number of variables in the fit ($N_{\text{var}} = 4$ to 5) was always lower than the number of independent points ($N_{\text{ind}} \sim 8$) as defined in IFEFFIT (Newville, 2001). nd = not determined because of too weak EXAFS signal.

1182 **Table 2.** Fraction of high-order silver chloride complexes ($\text{AgCl}_3^{2-} \pm \text{AgCl}_4^{3-}$) in the total
 1183 dissolved silver in the investigated aqueous solutions as inferred from the number of Cl
 1184 neighbors and Ag-Cl interatomic distances (Table 1), and its comparison with
 1185 thermodynamic predictions using available stability constants for Ag chloride species.
 1186

m_{Cl} mol/kg H_2O	T°C	% $[\text{AgCl}_3]$ from N_{Cl} ^(a)	% $[\text{AgCl}_3]$ from R_{Cl} ^(b)	% AgCl_3^{2-} Zot95 ^(c)	% AgCl_3^{2-} + AgCl_4^{3-} Sve97 ^(d)	% AgCl_3^{2-} Sew76 ^(e)
0.7	300	< 20	< 10	12	13	7
0.7	400	< 20	< 10	< 5	16	na
0.7	450	< 20	< 10	< 1	48	na
2.6	200	< 30	41	44	55	56
2.6	300	< 20	23	15	62	38
2.6	400	< 20	9	6	94	na
5.9	200	50	50	65	80	73
5.9	300	< 20	41	29	86	60
5.9	400	< 20	27	16	99	na
5.9	450	< 20	18	< 10	> 99	na
error		± 20	± 15	± 10	± 7	± 5

1187
 1188
 1189
 1190
 1191
 1192
 1193
 1194
 1195
 1196
 1197
 1198
 1199
 1200
 1201
 1202
 1203
 1204

(a) From average N_{Cl} value ± 0.2 Cl atoms (experimental EXAFS, this study, Table 1)

(b) From average R_{Cl} value ± 0.01 Å (Table 1) and adopting Ag-Cl distances of 2.38 ± 0.01 Å (experimental EXAFS, this study) and 2.60 ± 0.05 Å (FPMD calculations, this study) for AgCl_2^- and AgCl_3^{2-} , respectively.

(c) Using the HKF parameters of Ag^+ , AgCl^0 and AgCl_2^- from Akinfiev and Zotov (2001), which yield identical stability constants for these species as older works of the same group (Zotov et al., 1995; Tagirov et al., 1997), and using the stability constants of AgCl_3^{2-} reported in Zotov et al. (1995) to 350°C at P_{sat} . Because AgCl solubility data (Zotov et al., 1995; Tagirov et al., 1997) indicate a negligible effect of pressure on the solubility at T to at least 350°C and P to 500-1000 bar, the AgCl_3^{2-} stability constants at P_{sat} were assumed to be the same at our experimental pressure of ~600 bar. See Pokrovski et al. (2009a) for details on thermodynamic data for other fluid constituents and activity coefficient models.

(d) Sverjensky et al. (1997) using the HKF parameters for $[\text{AgCl}_{1-4}]$ complexes.

(e) Seward (1976) reported stability constants of AgCl_3^{2-} to 200°C at P_{sat} . We extrapolated according to his data the equilibrium constant of the pseudo-isocoulombic reaction $\text{AgCl}_2^- + \text{Cl}^- = \text{AgCl}_3^{2-}$ versus $1/T(\text{K})$ to 300°C and assumed that this constant is independent of pressure to at least 600 bars.

na = not applicable because requires too far extrapolations on temperature.

Table 3. Thermodynamic properties of silver chloride complexes from the literature, recommended on the basis of XAS analyses, FPMD simulations, and in-situ XAS measured AgCl(s) solubility of this study.

Species	Thermodynamic data	References
Ag ⁺ ^(d)	G ^(a) = 18427 cal/mol, S ^(b) = 17.54 cal/(mol K), HKF model coefficients: a ₁ ×10 = 1.7285 cal/(mol bar), a ₂ ×10 ⁻² = -3.5608 cal/mol, a ₃ = 7.1496 cal K/(mol bar), a ₄ ×10 ⁻⁴ = -2.6318 cal K/mol, c ₁ = 18.8783 cal/(mol K), c ₂ ×10 ⁻⁴ = -4.4327 cal K/mol, ω×10 ⁻⁵ = 0.2160 cal/mol	Akinfiyev and Zotov, 2001
AgCl ⁰ (aq) ^(d)	G = -17399 cal/mol, S = 32.067 cal/(mol K), HKF model coefficients: a ₁ ×10 = 4.2750 cal/(mol bar), a ₂ ×10 ⁻² = 3.7555 cal/mol, a ₃ = 4.2739 cal K/(mol bar), a ₄ ×10 ⁻⁴ = -2.9343 cal K/mol, c ₁ = 3.0441 cal/(mol K), c ₂ ×10 ⁻⁴ = -4.1199 cal K/mol, ω×10 ⁻⁵ = 0.00 cal/mol	Akinfiyev and Zotov, 2001
AgCl ₂ ⁻	G = -51350 cal/mol, S = 49.78 cal/(mol K), HKF model coefficients: a ₁ ×10 = 7.1327 cal/(mol bar), a ₂ ×10 ⁻² = 9.8065 cal/mol, a ₃ = 1.8947 cal K/(mol bar), a ₄ ×10 ⁻⁴ = -3.1844 cal K/mol, c ₁ = 4.8953 cal/(mol K), c ₂ ×10 ⁻⁴ = -6.7789 cal K/mol, ω×10 ⁻⁵ = 0.6667 cal/mol	Akinfiyev and Zotov, 2001
AgCl ₃ ²⁻	Reaction AgCl(s) + 2Cl ⁻ = AgCl ₃ ²⁻ log ₁₀ K = -2230.4/T(K) + 4.391 - 0.00528 T(K) (P _{sat} , 293-648 K) ^(c)	Zotov et al., 1995
Chlorargirite, AgCl(s)	G = -26247 cal/mol, S = 22.99 cal/(mol K), V = 25.727 cm ³ /mol, Heat capacity coefficients (cal units): 14.331 + 1.821×10 ⁻³ T(K) - 2.431×10 ⁻⁵ /T(K) ² (298-728 K)	Robie and Hemingway, 1995

^(a) G = standard molal Gibbs free energy of formation from the elements at 25°C, 1 bar

^(b) S = standard molal entropy at 25°C, 1 bar

^(c) Assumed to be valid to 1000 bar (see footnote of Table 2)

^(d) These species are included for consistency, but are minor in saline fluids compared to the di- and tri-chloride.

1219

Figure captions

1220 **Fig. 1.** Distribution of Ag-chloride species in an acidic aqueous solution as a function of NaCl concentration at
 1221 400°C and 800 bar, calculated using the thermodynamic properties of silver chloride complexes reported by (a)
 1222 Sverjensky et al. (1997; SUPCRT 2007, <http://geopig.asu.edu/index.html#>) and (b) Akinfiev and Zotov (2001),
 1223 both based on regressions of available experimental data within the framework of the revised HKF model.
 1224 Thermodynamic data for other fluid constituents and activity coefficient models are detailed in Pokrovski et al.
 1225 (2009a). Note significant differences in the Ag species distribution at NaCl concentration above 0.5m according
 1226 to these two main databases largely used by geochemists.

1227 **Fig. 2.** Solubility of argentite (Ag_2S , cubic) in a model aqueous fluid of 1.5m NaCl + 0.5m KCl (~25 wt% NaCl
 1228 equivalent) as a function of temperature at 1000 bar in equilibrium with the Pyrite-Pyrrhotite-Magnetite sulfur
 1229 fugacity buffer and Muscovite(\pm Andalusite)-Kfeldspar-Quartz acidity buffer, according to the two major
 1230 thermodynamic datasets for Ag chloride complexes, Sverjensky et al. (1997; SUPCRT
 1231 <http://geopig.asu.edu/index.html#>) and Akinfiev and Zotov (2001). Thermodynamic data for other fluid
 1232 constituents and activity coefficient models are detailed in Pokrovski et al. (2009a). Differences in Ag_2S solubility
 1233 attain a factor of 10 to 50 between 400 and 600°C. The inflexion of both solubility curves above 500°C is due to
 1234 the muscovite breakdown to andalusite, which leads to pH increase in the fluid at these conditions.

1235 **Fig. 3.** (a) Normalized k^2 -weighted EXAFS spectra of studied Ag nitrate and chloride solutions at 600-750 bars
 1236 and indicated temperatures (in °C), and (b) their corresponding Fourier Transform (FT) magnitudes (not corrected
 1237 for phase shift). Vertical dashed line in (a) is drawn to indicate the phase shift between O and Cl backscattering
 1238 atoms in nitrate and chloride solutions and temperature changes in Ag-Cl distances in chloride solutions. Vertical
 1239 dashed lines in (b) indicate approximate positions of O and Cl atoms in the first coordination shell of Ag (see
 1240 Table 1 for phase-corrected distances).

1241 **Fig. 4.** Average Ag-Cl distances (a) and number of Cl atoms (b) in the first silver coordination shell derived from
 1242 EXAFS analyses of chloride aqueous solutions as a function of temperature.

1243 **Fig. 5.** (a) Normalized XANES spectra at Ag K-edge of selected nitrate and chloride aqueous solutions and solid
 1244 reference compounds. (b) XANES spectra of representative AgO/Cl clusters of different stoichiometry and
 1245 geometry, calculated using the FDMNES code (Joly, 2001). Vertical lines on both panels indicate the major
 1246 spectral features discussed in section 3.2.

1247 **Fig. 6.** Comparison of calculated XANES spectra for the representative Ag-Cl clusters of different geometry and
 1248 degree of distortion with key experimental spectra: (a) AgCl_2 clusters ($R_{\text{Ag-Cl}} = 2.35 \text{ \AA}$) with different Cl-Ag-Cl
 1249 angles (in degrees in the figure legend) versus the experimental spectrum of the most dilute Cl solution at 450°C
 1250 (exp6_0.70m Cl); (b) AgCl_3 ($R_{\text{Ag-Cl}} = 2.55 \text{ \AA}$) and AgCl_4 clusters (R_{AgCl} mean $\sim 2.50 \text{ \AA}$, ΔR in the figure legend
 1251 indicates the difference between two pairs of Ag-Cl distances in the distorted tetrahedral-like cluster).

1252 **Fig.7.** Structures of stable Ag-Cl-O species identified by FPMD simulations with Ag-Cl interatomic distances (in
 1253 Å) and Cl-Ag-Cl angles (in degrees): (a) AgCl(H₂O), (b) AgCl₂⁻, (c) AgCl₃²⁻, d) AgCl₃(H₂O)²⁻, and e) AgCl₄³⁻.

1254 **Fig. 8.** Local environment of the AgCl₂⁻ species derived from FPMD simulations at 50°C, 1 bar and 380°C, 600
 1255 bar (with Cl:Ag ratio = 2 in the system). (a) Ag-Cl and Ag-O radial distribution functions, and (b) Cl-Ag-Cl
 1256 angular distributions. The amplitude of the Ag-Cl radial distribution functions in (a) is divided by 60 to allow
 1257 comparison with that of Ag-O.

1258 **Fig. 9.** Comparison of the MD-EXAFS spectrum of the AgCl₂⁻ species at 380°C, 600 bar with the experimental
 1259 spectrum obtained from 0.7m Cl solution at 400°C, 750 bar (exp#6). The MD calculated spectrum was scaled by
 1260 0.75 in amplitude (experimental amplitude reduction factor) and shifted along the k axis (non-structural Δe value
 1261 in EXAFS, see text) for better comparison.

1262 **Fig. 10.** MD-EXAFS spectra of (a) AgCl₂⁻ at 50°C/1 bar and 380°C/600 bar, and (b) AgCl₂⁻, AgCl₃²⁻, and AgCl₄³⁻
 1263 at 50°C/1 bar. The AgCl₃(H₂O)²⁻ spectrum (not shown) is close to that of AgCl₄³⁻. Note the strong similarity of the
 1264 spectra of AgCl₂⁻ and AgCl₄³⁻ (see text).

1265 **Fig. 11.** Solubility of AgCl(s) at 200°C and 600 bars measured in situ from the absorption edge height of
 1266 transmission spectra in this study (symbols) and its comparison with values calculated using available
 1267 thermodynamic data for Ag chloride complexes. The uncertainties of XAS measurements are comparable with the
 1268 symbol size. Aki01 – Akinfiev and Zotov (2001) for AgCl⁰ and AgCl₂⁻; Zot95 – Zotov et al. (1995) for AgCl₃²⁻;
 1269 Sew76 – Seward (1976) for [AgCl₁₋₃] complexes; Sve97 – Sverjensky et al. (1997) for [AgCl₁₋₄] complexes.

1270 **Fig. 12.** Solubility of argentite, native gold, and chalcopyrite (a) as a function of temperature in a model aqueous
 1271 solution of 10 wt% NaCl equivalent at pH 5 in equilibrium with the pyrite-magnetite-hematite oxygen and sulfur
 1272 fugacity buffer at pressures progressively decreasing from 1500 bar at 450-550°C to 200 bar below 250°C; b) as a
 1273 function of pH at 400°C, 500 bar, 10 wt% NaCl, in equilibrium with pyrite-magnetite-hematite; c) as a function of
 1274 salinity at 400°C, 500 bar, pH 5, in equilibrium with pyrite-magnetite-hematite; d) as a function of H₂S
 1275 concentration at 400°C, 500 bar, 10 wt% NaCl, pH 5, and oxygen fugacity of the magnetite-hematite buffer.
 1276 Calculations were performed using the HCh computer code (Shvarov, 2008). Thermodynamic properties of the
 1277 minerals are taken from SUPCRT (Johnson et al., 1992), those of major fluid constituents and activity coefficient
 1278 models are detailed in Pokrovski et al. (2009a,b). Stability constants of Ag, Cu, and Au aqueous chloride and
 1279 sulfide complexes are from Zotov et al. (1995) for AgCl₃²⁻, Akinfiev and Zotov (2001) for AgCl₂⁻ and CuCl₂⁻,
 1280 Akinfiev et al. (2008) for AgHS, Ag(HS)₂⁻, CuHS, Cu(HS)₂⁻, AuHS, and Au(HS)₂⁻, and Pokrovski et al. (2009a)
 1281 for AuHS(H₂S). These thermodynamic datasets are in good agreement with the major experimental data sources.
 1282 The dominant aqueous species for each metal are indicated.

Figure 1

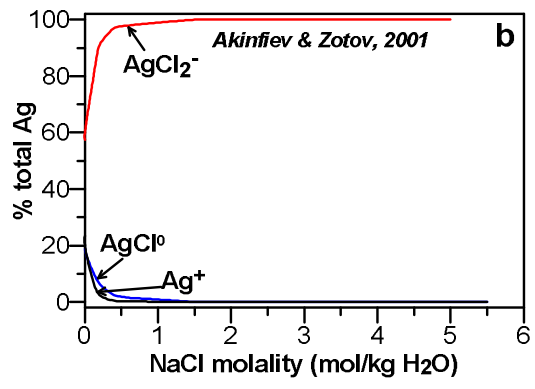
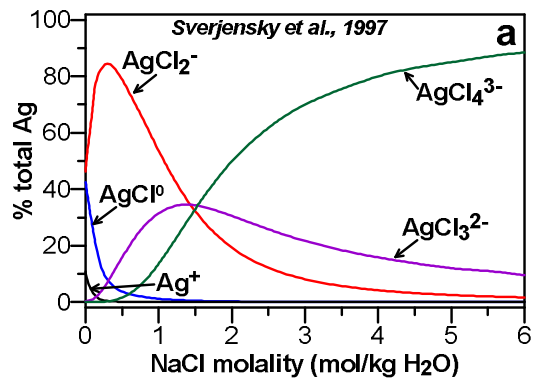
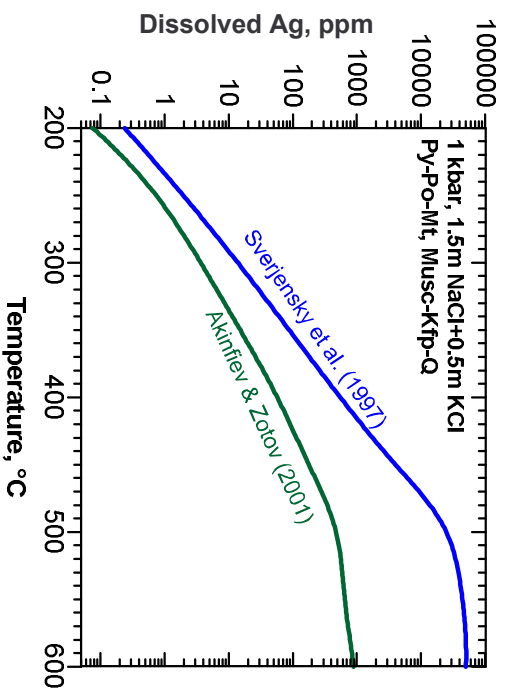


Figure 2



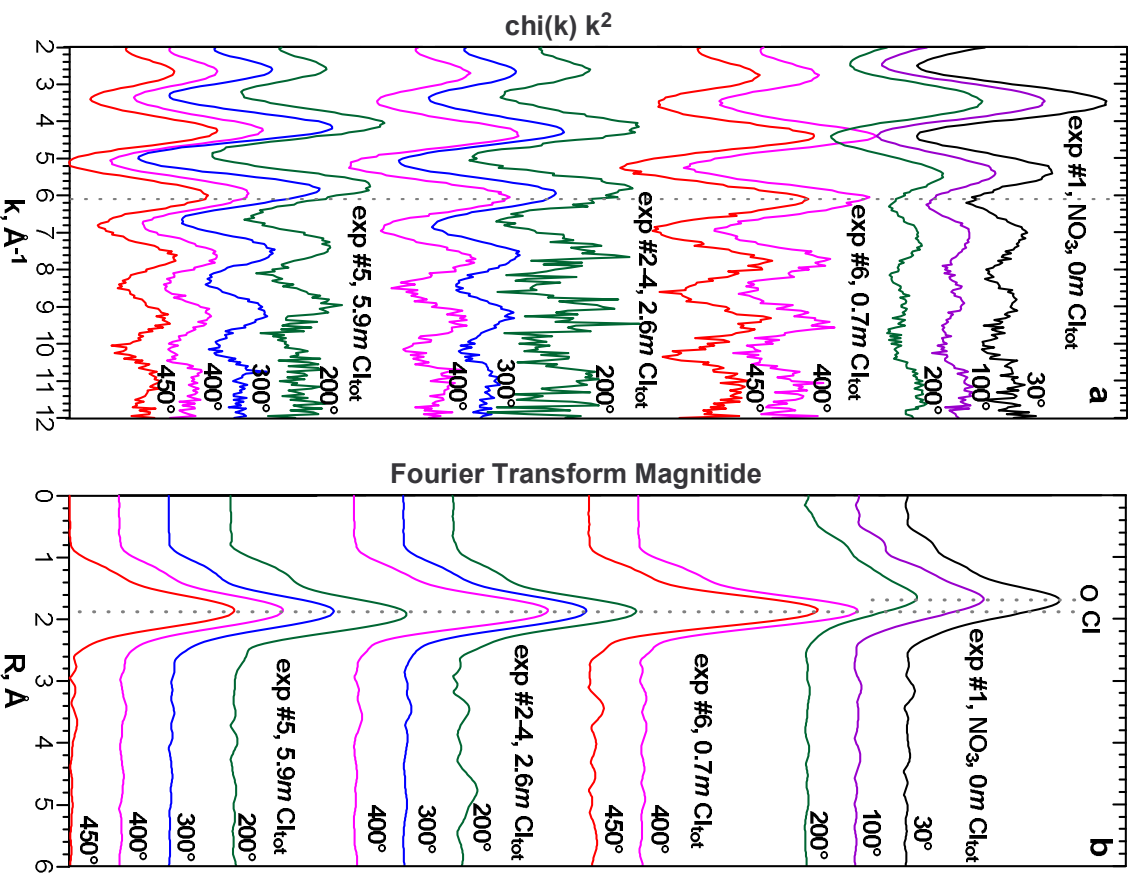


Figure 4

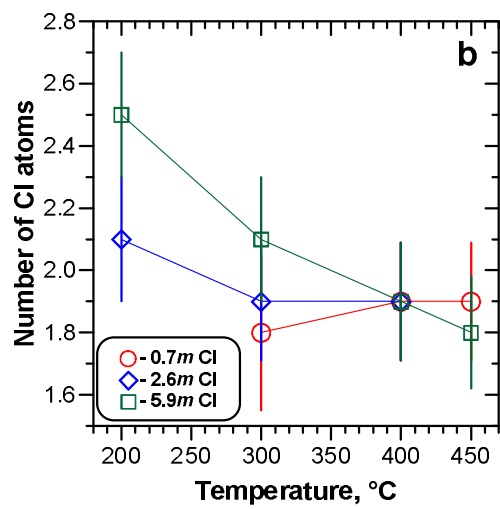
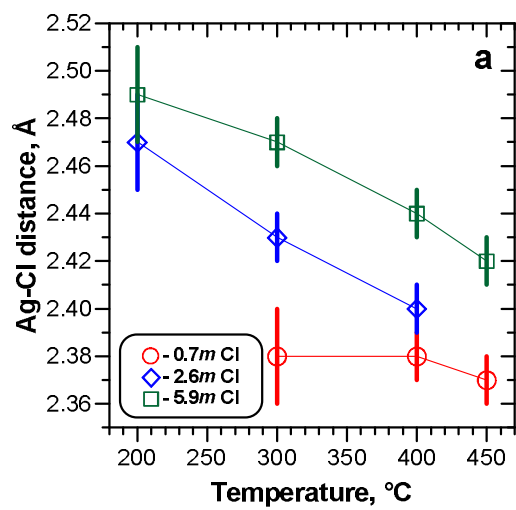


Figure 5

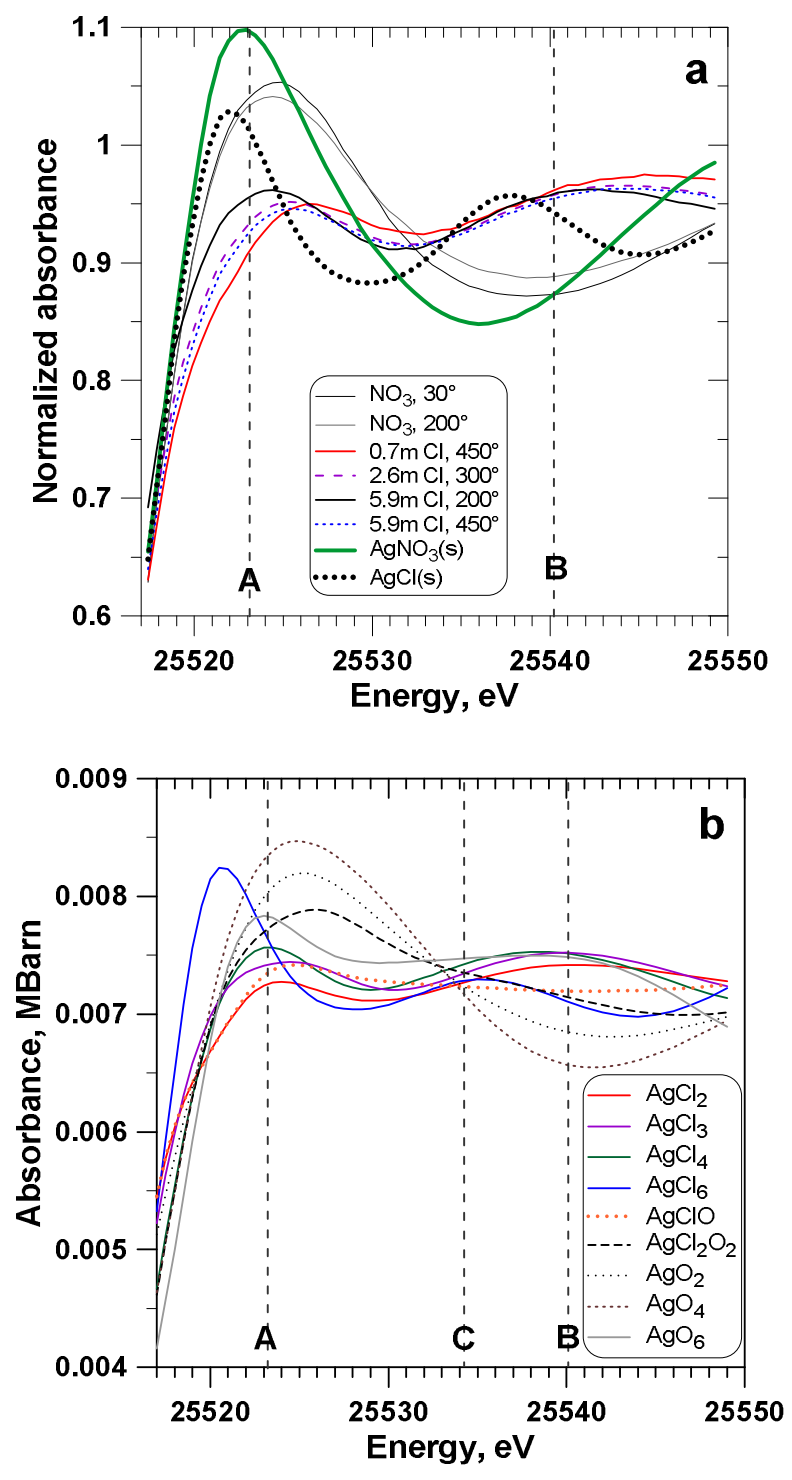


Figure 6

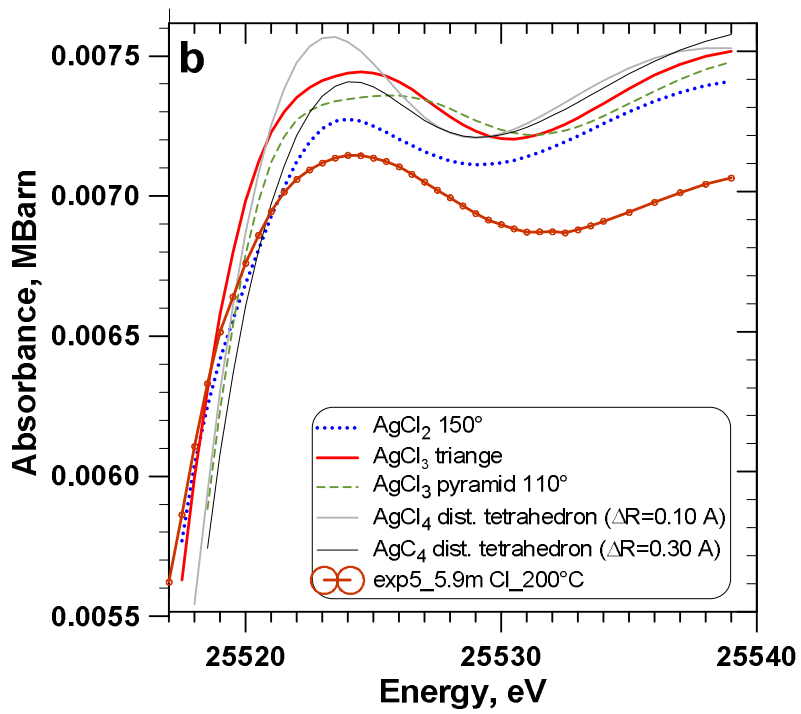
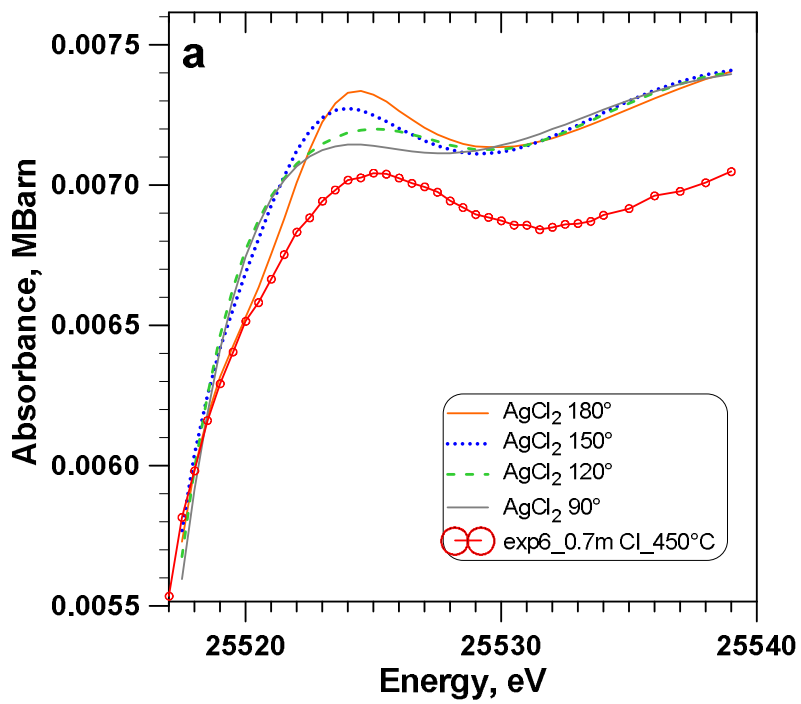


Figure 7

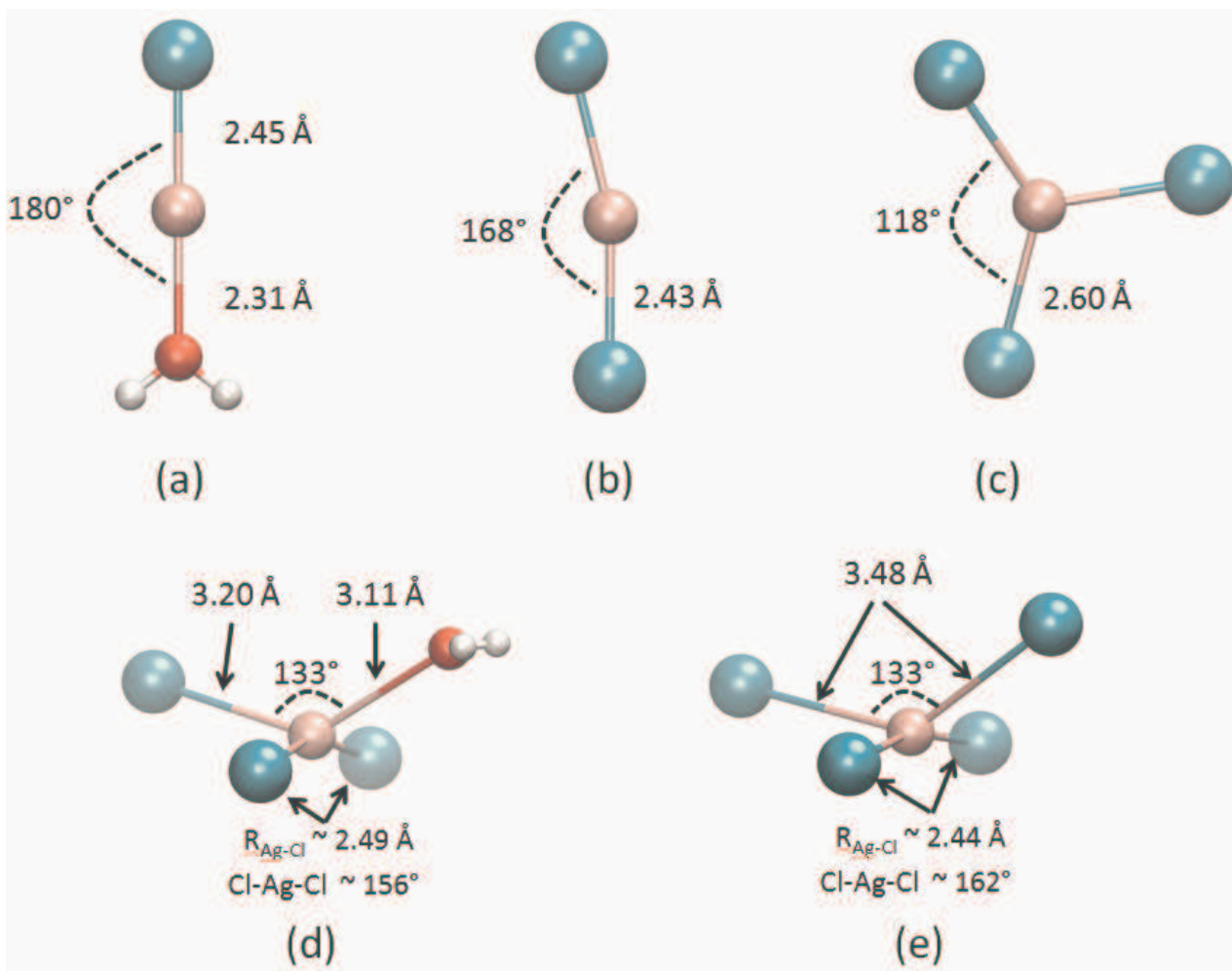


Figure 8

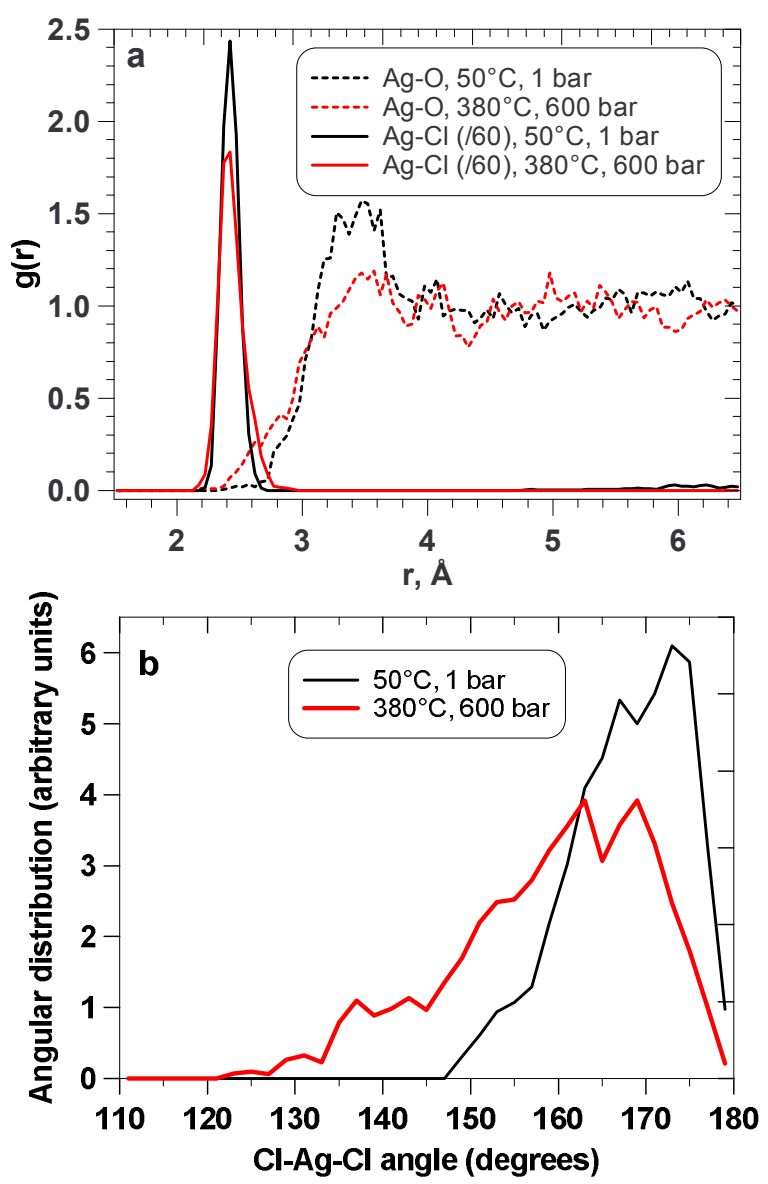


Figure 9

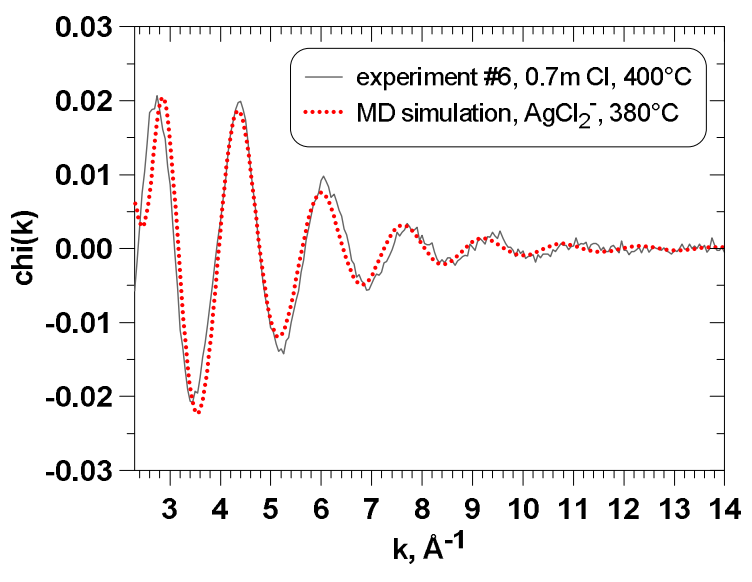
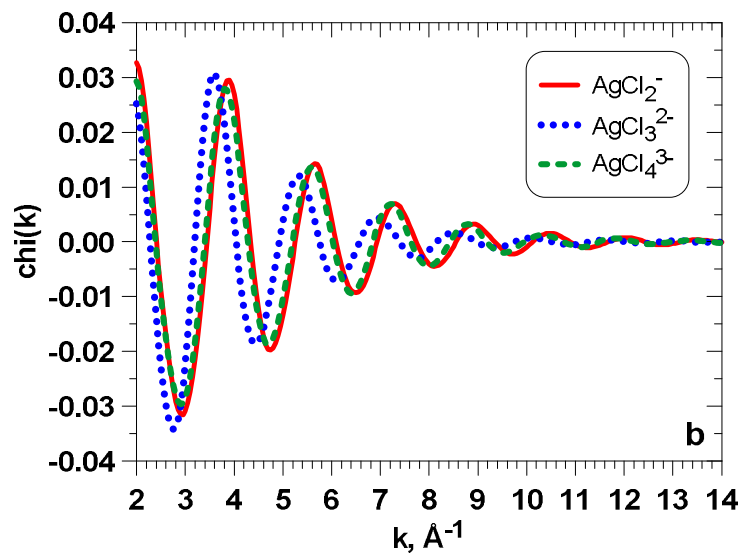
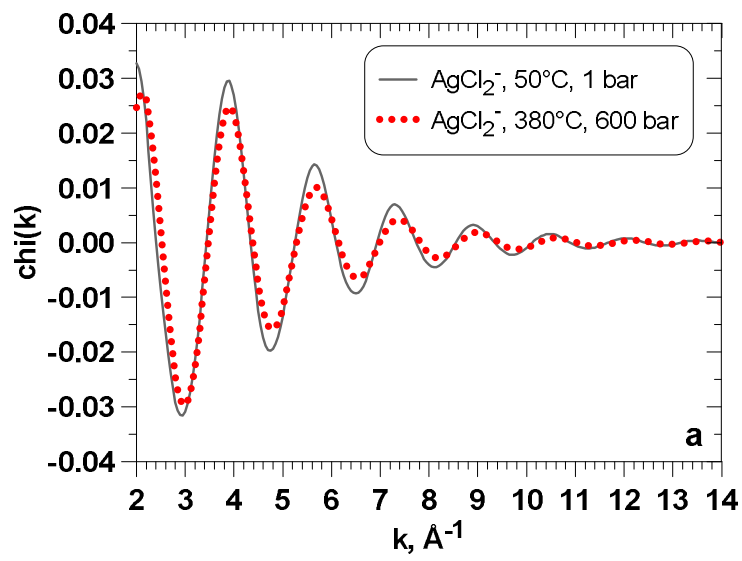


Figure 10



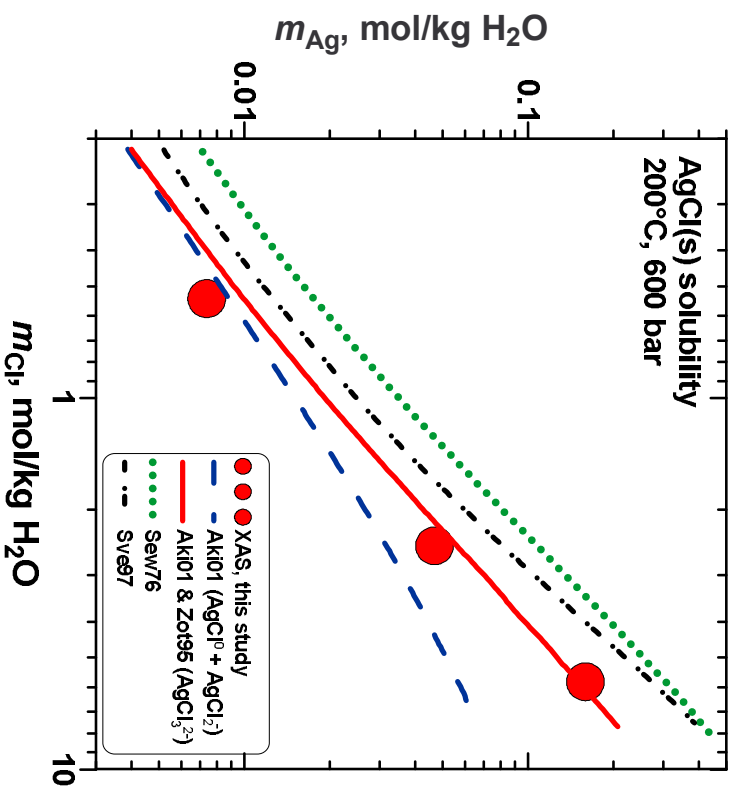
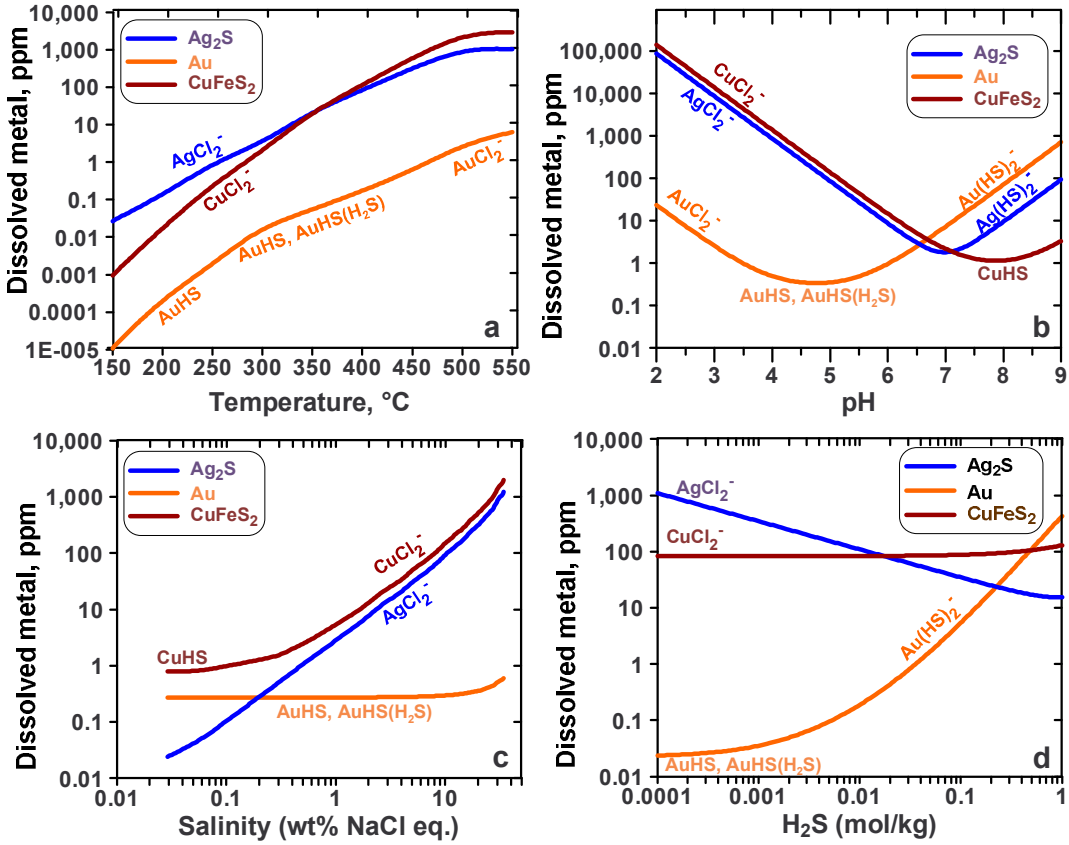


Figure 12



Electronic Annex

[Click here to download Electronic Annex: ElectronicAnnex_revised_nov12.pdf](#)